THEORIES OF HOT-PRESSING: PLASTIC FLOW CONTRIBUTION

BY

A. SADANANDA RAO

B.Sc., University of Mysore, India, 1965
B.E. (Metallurgy), I.I.Sc., Bangalore, India, 1969

A THESIS SUBMITTED IN PARTIAL FULFILMENT OF

THE REQUIREMENTS FOR THE DEGREE OF

MASTER OF APPLIED SCIENCE

in the Department

of

METALLURGY

We accept this thesis as conforming to the

required standard

THE UNIVERSITY OF BRITISH COLUMBIA
August, 1971

In presenting this thesis in partial fulfilment of the requirements for an advanced degree at the University of British Columbia, I agree that the Library shall make it freely available for reference and study. I further agree that permission for extensive copying of this thesis for scholarly purposes may be granted by the Head of my Department or by his representatives. It is understood that copying or publication of this thesis for financial gain shall not be allowed without my written permission.

Department of Metallurgy

The University of British Columbia
Vancouver 8, Canada

Date 22nd Sept 1971

ABSTRACT

The contribution of plastic flow to overall densification of a powder compact during hot-pressing has been analysed. The basis of this analysis is the incorporation of hot-working characteristics of materials at elevated temperatures into an equation applicable to hot-pressing conditions. The empirical equation relating steady state strain rate to stress is $\dot{\varepsilon} = A\sigma^n$ and for the densification of a powder compact, the strain rate $\dot{\varepsilon} = \frac{1}{D}\frac{dD}{dt}$.

The particles are assumed to be spheres and four different packing geometric configurations: cubic, orthorhombic, rhombic dodecahedron and b.c.c. are considered. Taking into consideration the effective stress acting at the points of contact, the equations for the strain rate can be combined and arranged into another equation which is shown below:

$$\int_{D_o}^{D_{max}} D^{-1}\{D^{2/3}\beta^{2/3}R^2-1\}^n dD = \int_o^t A\left(\frac{\sigma}{\alpha_1}\right)^n dt$$

where α_1 and β are geometric constants and can be calculated from the packing geometry. 'A' and 'n' are material constants. D is the relative density of the compact, and 'R' is the radius of sphere at any stage of deformation in arbitrary units.

Computerized plots of D vs t were obtained for lead-2% antimony, nickel and alumina. Experimental verification of these plots was carried out using hot-pressing data for lead-2% antimony, nickel and alumina spheres. The hot-compaction experiments were carried out over a range of temperatures for each material and under different pressures.

The experimental data fitted well with the theoretical prediction for the orthorhombic model. However, a deviation at the initial stage

of compaction was encountered in most cases. This deviation was explained on the basis of the contribution to densification by particle movement or rearrangement at the initial stage, which could not be taken into account in the theoretical derivation.

The stress concentration factor i.e., the effective stress acting at necks between particles has been calculated. This was found to be very much higher than that previously used by other workers. The theoretical equation for the effective stress is

$$\sigma_{eff} = \frac{\sigma}{\alpha_1(D^{2/3}\beta^{2/3}R^2-1)}$$

This equation predicts an effective stress, which is more than an order of magnitude higher than that predicted by several empirical equations used previously.

TABLE OF CONTENTS

LIST OF FIGURES

LIST OF TABLES

ACKNOWLEDGEMENT

The author is grateful for the advice and encouragement given by his research director Dr. A.C.D. Chaklader. Thanks are also extended to other faculty members and fellow graduate students for many helpful discussions. Financial assistance from the National Research Council (NRC Grant No. A-2461) is gratefully acknowledged.

CHAPTER I

INTRODUCTION

Hot-pressing refers to densification of a powder compact under pressure at elevated temperatures. It is usually conducted at a temperature several hundred degrees below the temperature at which sintering is carried out (without any external pressure). Hot-pressing has gained importance as a commercial process since one can achieve greater density at lower temperatures and shorter times than in conventional sintering, and with much more microstructural control.

The densification of powder compacts during hot-pressing has been generally studied as a function of temperature, pressure and time. For kinetic analysis, the change of relative density (or bulk density) as a function of time under isothermal conditions and at a constant pressure is usually determined. A typical densification curve is shown schematically in Figure 1, where the relative density vs time is plotted at a constant temperature and pressure. Three distinct regions are recognised on the curve. The extent of the contribution from each of the three mechanisms of mass transport, i.e. particle rearrangement with or without fragmentation, plastic flow, and diffusion, depends on the type of material, the temperature and the stress level used during hot-pressing. For example, brittle solids in a compact at relatively

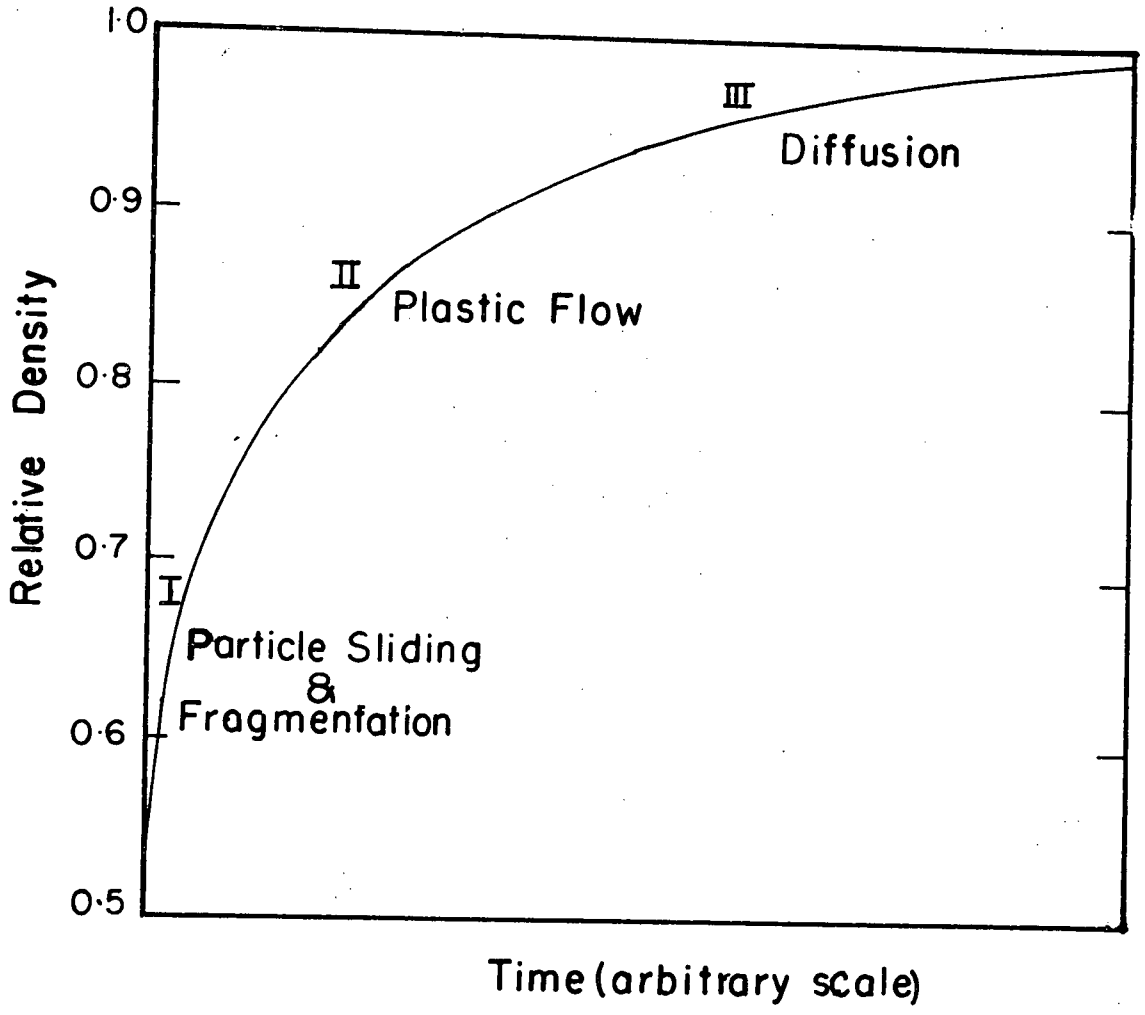

Figure 1. A schematic densification curve.

low temperature tend to fracture as soon as a load is applied during hot-pressing. The densification is primarily achieved by fragmentation and particle movement. This will be followed by plastic flow, only if the temperature and stress are high enough that dislocations can move. If no diffusional process occurs after this stage, the compact will reach an "end-point density" which is below its theoretical density. Metal powder compacts can be expected to have a much greater contribution to densification from plastic flow than ceramic oxides. Also, plastic flow would in general be a significant contributing factor to densification at high temperatures and high stresses.

The different mechanisms of material transport which can be expected to be predominant in various materials and in wide ranges of temperature and pressure are summarized in Table 1.

I.1 Densification Due to Particle Rearrangement and Fragmentation

Felten[6] carried out a number of hot-pressing investigations with Al_2O_3 having three different average particle sizes (0.05 μ, 0.3 μ and 5-10 μ). He conducted all his experiments at low temperatures (750-1300°C) to minimize the contribution from plastic flow and diffusion to densification. His data fitted well with a plastic flow equation, developed by Murray, Livey and Williams,[19] but only at the later stages of densification. There was a large deviation at the initial stage of densification from the theoretical prediction. He concluded that that this deviation at the very early stage must be attributed to another mode of densification which he called particle rearrangement. This rearrangement may also be associated with fragmentation.

Table 1. Predominant Mechanisms of Densification under Given Hot-Pressing Conditions.

Fracture	Low temperature
	High pressure
Plastic flow	Large particle size
Boundary diffusion	High temperature
	Low pressure
Lattice diffusion	Small particle size

Similarly Chang and Rhodes,[1] who studied the microstructures of uranium-carbide powder compacts after hot-pressing in the temperature range 500 to 1500°C under pressures varying from 10,000 to 46,000 atmospheres, concluded that particle sliding and fragmentation played a significant role in the initial stage of densification.

I.2 Densification Due to Plastic Flow

Among the contributions to the theory of hot-pressing, the best known is perhaps that of Murray, Rodger and Williams (also Murray, Livey and Williams)[19] who modified the sintering theory of Mackenzie and Shuttleworth to explain the observed behaviour in hot-pressing, of various oxides and carbides. The final form of the equation, neglecting the contribution from sintering, is

$$\frac{dD}{dt} = \frac{3P}{4\eta}(1-D) \qquad (1a)$$

where D is the relative density at time t, P is the applied pressure and η is the viscosity. It was assumed by Mackenzie and Shuttleworth[8] that all solids can be divided into two groups - Newtonian and Bingham. As metals and oxides can only flow above a critical stress, they approximated the crystalline solids as the "Bingham solid ". Hence, equation (1a) contains a viscosity term. Their plastic flow theory succeeded in explaining the increased rate of densification with pressure and the effect of pressure on end point density at a constant temperature.

Mangsen, Lambertson and Best[16] studied the hot-pressing characteristics

of aluminum-oxide to understand the mechanisms involved in the densification process. They observed that their experimental data fitted very well with the Murray, Livey and Williams[19] equation. The viscosity values were calculated from these data as a function of temperature which closely agreed with the values reported in the literature.

Murray's[19] equation has also been employed by Vasilos[25] to interpret the data obtained during hot-pressing of fused silica. He used the integrated form of equation 1a, as follows:

$$-\ln(1-D) = \frac{3P}{4\eta} t + c \qquad (1b)$$

when $t = 0$; $D = D_o$ (the initial pressed density). So the integration constant c equals $-\ln(1-D_o)$. He plotted $-\ln(1-D)$ vs time, as shown in Figure 2. The linear relation between these two quantities is essentially observed regardless of differences in particle size, applied pressure, or temperature. Viscosity values computed from the slopes of these curves agreed reasonably well with those reported in the literature.

McClelland[17] modified Murray's equation to fit his hot-pressing data for BeO and Al_2O_3, taking into account the change of effective pressure which accompanies closing the pores. Equation 1a can be used to describe the variation of density with time only if pressure remains constant during hot-pressing. The pressure which is effective in closing the pores, however, is not equal to the applied pressure. Due to the presence of the voids, whose size changes during the hot-pressing operation, the area over which the applied load is transmitted increases with increasing density. Thus, the pressure

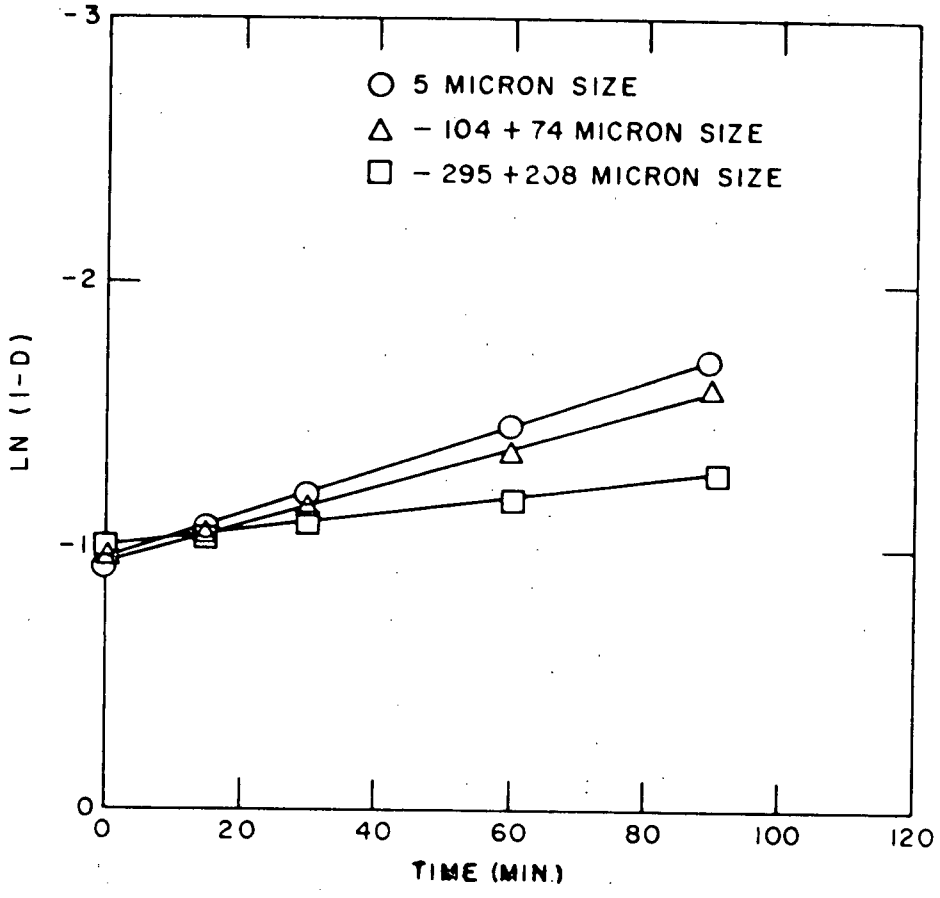

Figure 2(a). Plot of ln(1-D) vs. time for fused silica at 1100°C and pressure of 1000 psi (after Vasilos[25]).

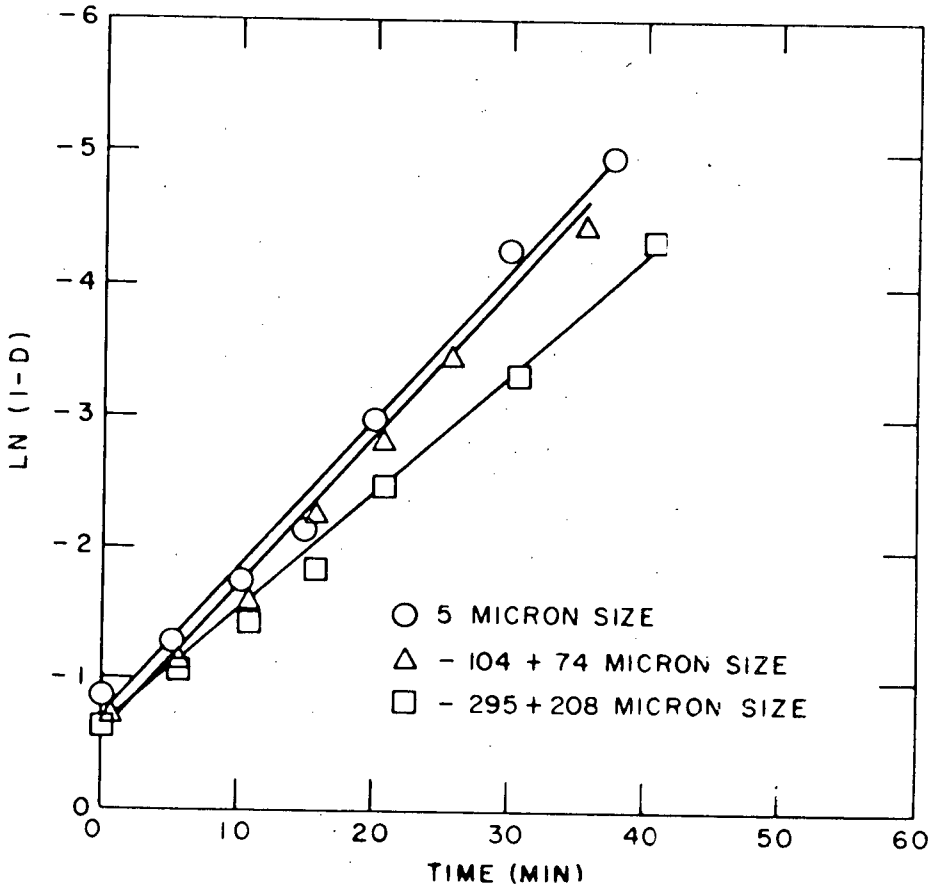

Figure 2(b). Plot of ln(1-D) vs. time for fused silica at 1150°C and pressure of 1000 psi (after Vasilos[25]).

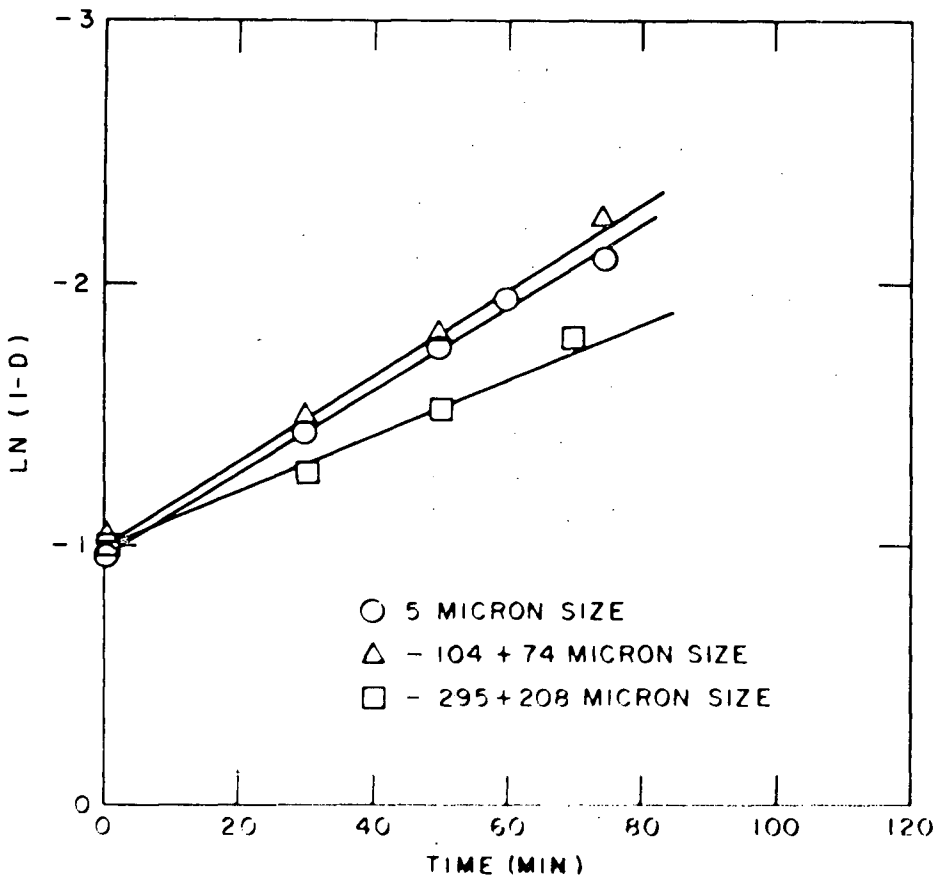

Figure 2(c). Plot of ln(1-D) vs. time for fused silica at 1100°C and pressure of 2500 psi (after Vasilos[25]).

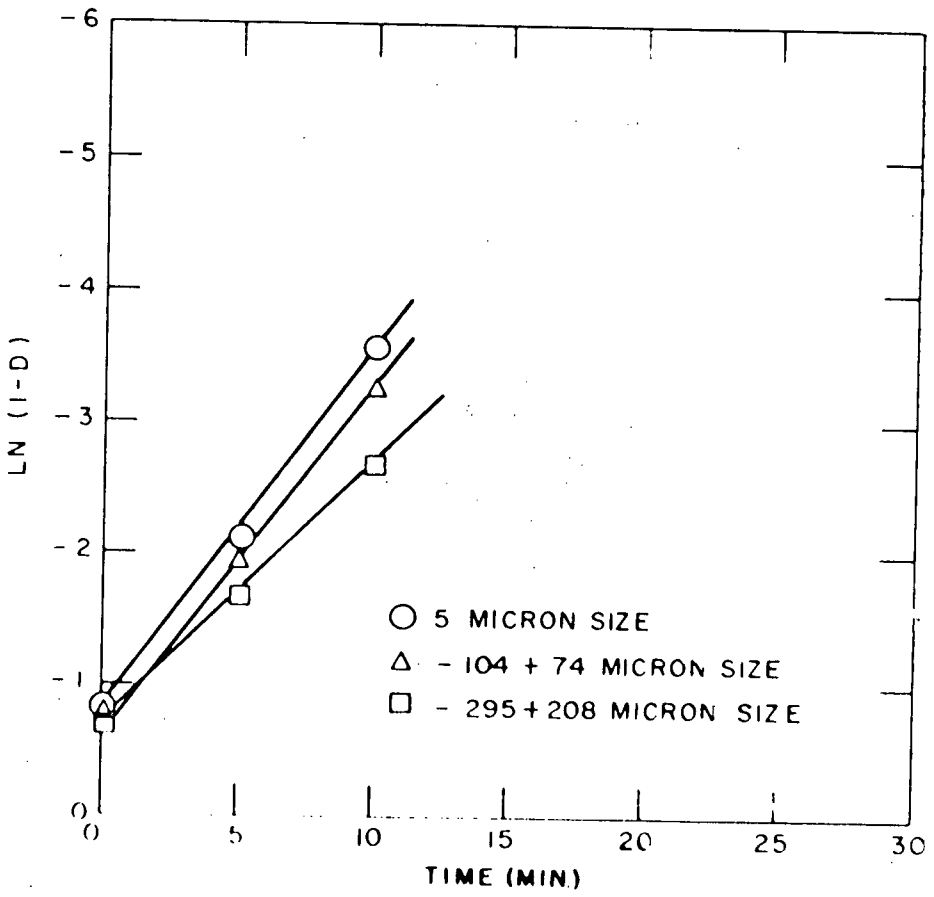

Figure 2(d). Plot of ln(1-D) vs. time for fused silica at 1150°C and pressure of 2500 psi (after Vasilos[25]).

effective in closing the pores is a function of porosity. McClelland's[17] final form of equation is as follows:

$$\int_{D_o}^{D} (dD/x\{\ln[1/(1-x^{2/3})] + a \ln x\}) = Kt \qquad (1c)$$

where x is (1-D), D is the density at time t

D_o = the initial density

$a = \sqrt{2}\ \tau_c/P$

$K = \frac{3P}{4\eta}$

τ_c = yield stress

P = pressure

η = viscosity.

The lefthand side of equation 1c can be integrated grapically for different values of D. McClelland[17] found good agreement between the theoretical curves and experimental data as is shown in Figure 3.

Kakar and Chaklader[12] developed a mathematical model for interpretations of densification due to plastic flow. Knowing the geometry of the particle and packing configuration in a die, they calculated the change of density of a compact of spheres produced by deformation at the points of contact of the spheres. For this calculation, several configurations were considered; cubic (Z = 6), hexagonal prism (Z = 8), rhombic dodecahedron (Z = 12) and tetrakaidecahedron (Z = 14) where Z is the coordination number. These are shown in Figure 5.

Due to indentation at the point of contact between two spheres as shown in Figure 5a, material will be transferred to fill the void space and this will increase the density of the compact. The final

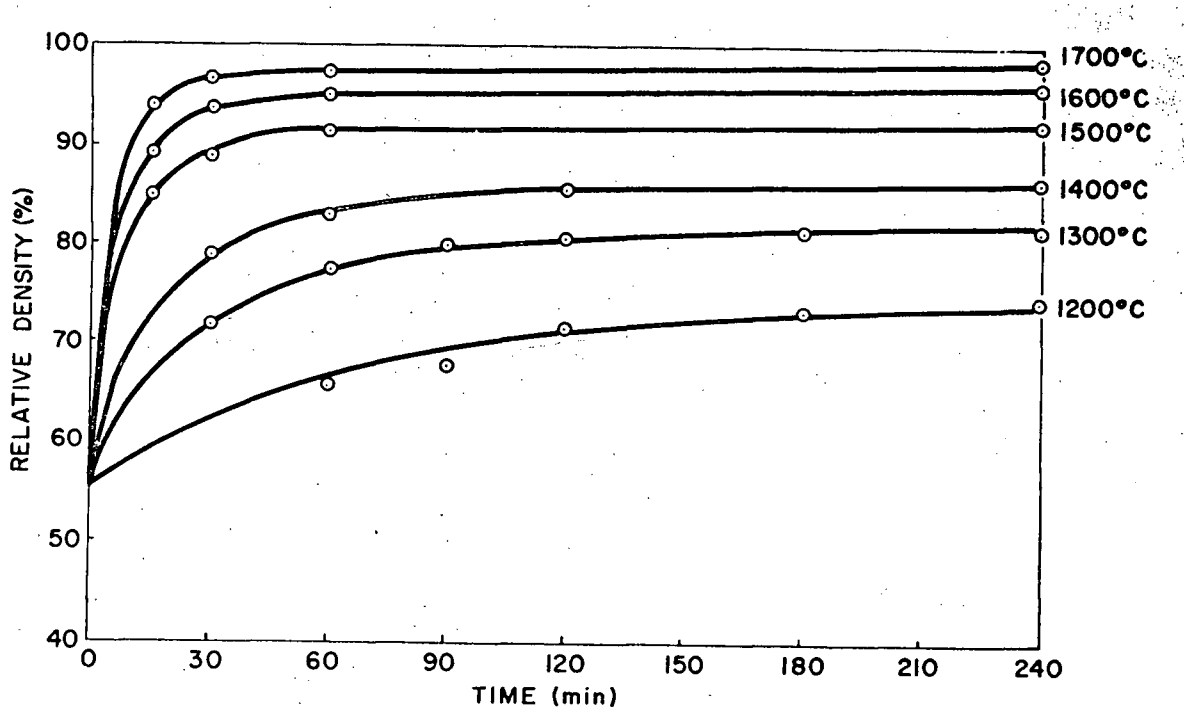

Figure 3. Temperature dependence of density of BeO while hot-pressing at 4000 psi (after McClelland[17]).

density due to these indentations at several points of contact (depending upon Z) is given as follows:

$$D - D_o = 3/2\ D_o(\frac{a}{R})^2 \quad (\text{at } \frac{a}{R} < 0.3) \tag{2a}$$

or

$$D - D_o = 101.5 \log Z\ (\frac{a}{R})^2 \tag{2b}$$

where Z = 6, 8 and 12; D and D_o are the relative densities of the compact at a > 0 and at a = 0 respectively, a is the radius of the flat face produced by indentation, and R is the radius of the sphere at any stage of densification. Kakar and Chaklader[12] tested this equation using hot-compaction data for lead, K-monel and Al_2O_3 spheres and they obtained a very good fit with the theoretically predicted values of the hexagonal prismatic model.

They introduced pressure and temperature dependent terms into equations 2a and 2b by considering that deformation at the points of contact between two particles is essentially a self-indentation process. Using the yielding criterion of Hencky[9] and Ishlinsky[10] for indentation i.e., the stress (σ_Y) necessary for yielding during indentation is three times the yield stress (Y) of the material, the effective stress acting on each face (σ_e) and the coordination number 8 (corresponding to 0.60 relative density of green compact), equation (2a) was transformed to give

$$D - D_o = \frac{D_o \sigma}{5Y} \tag{2c}$$

An exponential temperature dependence of the yield strength modifies equation 2c into

$$D - D_o = \frac{D_o \sigma \exp(Q/RT)}{5A} \qquad (2d)$$

In this equation σ is the applied pressure, A is a pre-exponential constant and Q is the activation energy for yielding.

Rummler and Palmour[22] studied the densification kinetics of magnesium-aluminate spinel during vacuum hot-pressing. They observed that below 1350°C, the densification kinetics of the spinel compacts were in agreement with Murray's expression which in its integral form predicts a linear relation between log porosity and time. Hence they concluded that the densification of magnesium-aluminate spinel below 1350°C was mainly due to plastic flow.

I.3 Densification Due to Diffusional Mass Transport

Koval'Chenko and Samsonov[14] proposed a hot-pressing equation based on the Nabarro-Herring[20] creep mechanism, which was verified by studies on tungsten-carbide and chromium-carbide. Scholz and Lersmacher[23] simplified Koval'Chenko and Samsonov's[14] equation and showed that it took a form similar to the equation developed by Murray et al.[19] viz

$$-\frac{dQ}{dt} = \frac{3P}{4\eta} Q$$

where Q = porosity.

Coble and Ellis[2] carried out hot-pressing experiments on aluminum single crystal spheres at 1530°C. They measured the effect of load on

initial neck growth between single crystal spheres and observed that the neck areas were larger than those of sintered spheres and that they were constant for all times between 10 and 480 minutes. They calculated the plastic flow contribution to the densification during hot-pressing. This calculation was based on the hydrostatic nature of stress and the geometric relations between particles. From this they found that for aluminum oxide the contribution of plastic flow to densification at the pressures normally used in hot-pressing was small. Hence they concluded that the final stage of densification of alumina occurs by enhanced diffusion under the influence of stress.

Rossi and Fulrath[21] also studied the kinetics of the final stage of densification of alumina under vacuum hot-pressing conditions. They suggested that plastic flow may be operative at an intermediate stage but definitely not during the final stage where diffusion-controlled creep was proposed to be the mechanism responsible for densification.

Vasilos and Spriggs[26] calculated the apparent bulk diffusion coefficients from the densification data for alumina and magnesia during hot-pressing and obtained an order of magnitude higher values for pressureless sintering. When the pressure correction term due to changing porosity was introduced into their calculations, their calculated diffusion-coefficients were in better agreement with those obtained from the sintering data. From these observations they concluded that the densification of a hot-pressed compact, beyond the initial stage is a diffusion controlled process.

A new treatment, proposed by Fryer[7] for the final densification step during hot-pressing, was based on a model involving the bulk diffusion

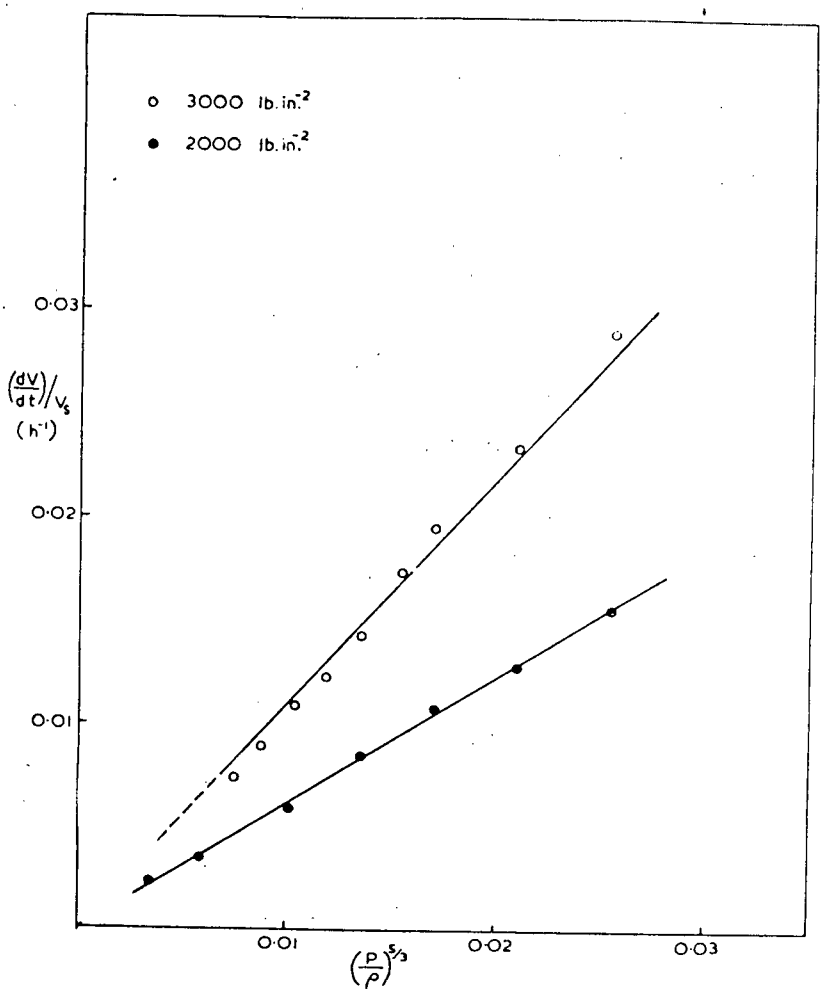

Figure 4(a) Shrinkage plots of alumina pressed at 1300°C, 2000, and 3000 psi (after Fryer[7]).

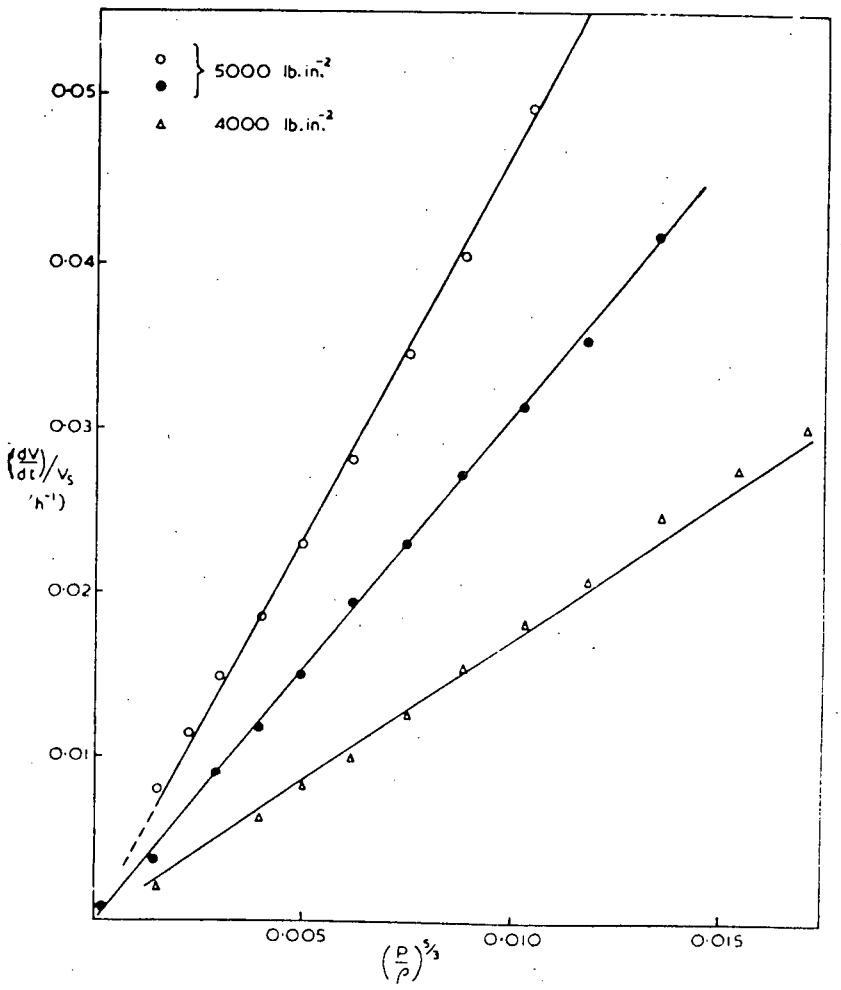

Figure 4(b). Shrinkage plots of alumina pressed at 1300°C, 4000, and 5000 psi (after Fryer[7]).

Table II. Densification Equations Based on Diffusional Mass Transport.

$(\frac{\Delta L}{L_o})^{5/2} = \frac{80\ D_1 L \Omega}{2\pi d^4\ KT}$	$\sigma = L/\pi x^2$ x = neck radius	Coble and Ellis[2]
$\frac{dD}{dt} = \frac{40\ D_1 \Omega b \sigma}{KT\ d^2}(1-D)$	N-H creep model	Rossi and Fulrath[21]
$D = \frac{\dot{\varepsilon} R^2 KT}{\sigma_c\ 4\Omega}$	$\sigma_c = \sigma(1 + 2P)$ $\dot{\varepsilon} = \frac{dP}{dt}$	Vasilos and Spriggs[26]
$\frac{1}{V_s}\frac{dV_s}{dt} = -Z\frac{\sigma}{d^2}\frac{D_1\Omega}{KT}(\frac{P}{D})^{5/3}$		Fryer[7]
$\frac{1}{D}\frac{dD}{dt} = \frac{40\ D_1\Omega}{3d^3\ KT}(\frac{\sigma}{D} + \frac{2\gamma}{r})$	lattice diffusion	Coble[4]
$\frac{1}{D}\frac{dD}{dt} = \frac{7.5\ D_b W}{d^3\ KT}(\frac{\sigma}{D} + \frac{2\gamma}{r})$	boundary diffusion	Coble[4]

where L = load
D = relative density
D_1 = bulk diffusion coefficient
D_b = boundary diffusion coefficient
Ω = vacancy volume
σ = applied stress
σ_c = effective stress
b = a stress-intensity factor
d = grain diameter
W = grain boundary width
R = grain radius
K = Boltzmann constant
T = temperature in °Kelvin
V_s = volume of solid
Z = a numerical constant
P = porosity = (1 - D)
$\dot{\varepsilon}$ = strain rate
γ = surface energy

of vacancies. The final form of his equation is shown in Table II. He tested his equation with hot-pressing data for alumina powder at 1300°C. The experimental data fitted well with the theoretical prediction, as shown in Figures 4a&4b.

Coble[4] has also developed a model for the final stage of densification of a powder compact, which explicitly includes both the surface energy and applied pressure as the driving force. This model is based on a steady state diffusive flow of material between concentric spherical shells. The driving force is expressed as follows

$$D.F = \frac{2\gamma}{r} + \frac{P_a}{D}$$

where P_a = applied force

γ = surface energy

D = relative density

r = radius of closed pore.

The resulting equations are also shown in Table II. Coble[4] concluded that this new approach should be able to predict densification up to the theoretical density of a powder compact.

I.4 Objectives of the Present Work

The contribution of plastic flow to densification during hot-pressing has been a subject of controversy. Although it has been accepted that plastic flow occurs at a certain stage during hot-pressing, which primarily depends on the temperature used, the extent of densification arising from any plastic flow mechanism has not been unambiguously determined.

The aim of this work was to study quantitatively the extent of densification by plastic flow during hot-pressing. Generally hot-pressing is carried out $\sim 0.6\ T_m$ (where T_m is the melting point in °K) of the material concerned. This is also approximately the hot-working temperature of the material. With this observation, an attempt has been made to derive an equation based on steady-state hot-deformation and subsequently test the equation with hot-compaction data for both metallic and non-metallic materials.

CHAPTER II

THEORETICAL FORMULATIONS

It has been found experimentally[11] that for a large number of materials, the steady-state strain rate is related to stress by a power law as follows

$$\dot{\varepsilon} = A \sigma_1^{n} \tag{3}$$

and the strain rate during densification of a powder compact (in a die) is approximately given by

$$\dot{\varepsilon} = \frac{-dh}{hdt} = \frac{1}{D}\frac{dD}{dt} \tag{4}$$

where "D" is the relative density, "h" is the instantaneous compact height; "A" is a constant at constant temperature; "n" is a material constant and σ_1 is the stress. For a compact this stress changes with densification during hot-pressing.

In the development of the theory, it is assumed that the particles in a compact are monosized spheres and that they are arranged in a regular three-dimensional array. During hot-pressing, they deform plastically, at the points of contact (necks) and form flat faces. The compacts' density change, as a result of this deformation, with

respect to neck radius, has been derived by Kakar and Chaklader[12] and is given by

$$D = \frac{1}{\beta(R^2-a^2)^{3/2}} \qquad (5)$$

D is the relative density of compact at neck radius "a", "R" is the instantaneous radius of the particle at neck radius "a" and β is a geometric constant which depends on the packing configuration. The effective stress acting on a compact will be affected by the packing geometry.

II.1 Theoretical Models

The deformation geometries of two spheres in contact and other simple geometric configurations are shown in Figure 5. Only four deformation models were considered - (1) simple cubic (Z = 6), (2) orthorhombic (Z = 8), (3) body-centred cubic (Z = 8), and (4) rhombohedral (Z = 12), where Z is the coordination number. The b.c.c. packing is an unstable arrangement in a unidirectional field of force (i.e. gravitational force). For theoretical purposes, it is assumed that each type of packing is stable and maintains its symmetry on the application of pressure, and that the material at the points of contact spreads symmetrically during deformation to maintain the sphericity of the particle.

The applied load can be considered to be acting on the whole unit cell where the unit cell is defined as a space-filling polyhedron with a deformed sphere situated inside the polyhedron (alternatively, the

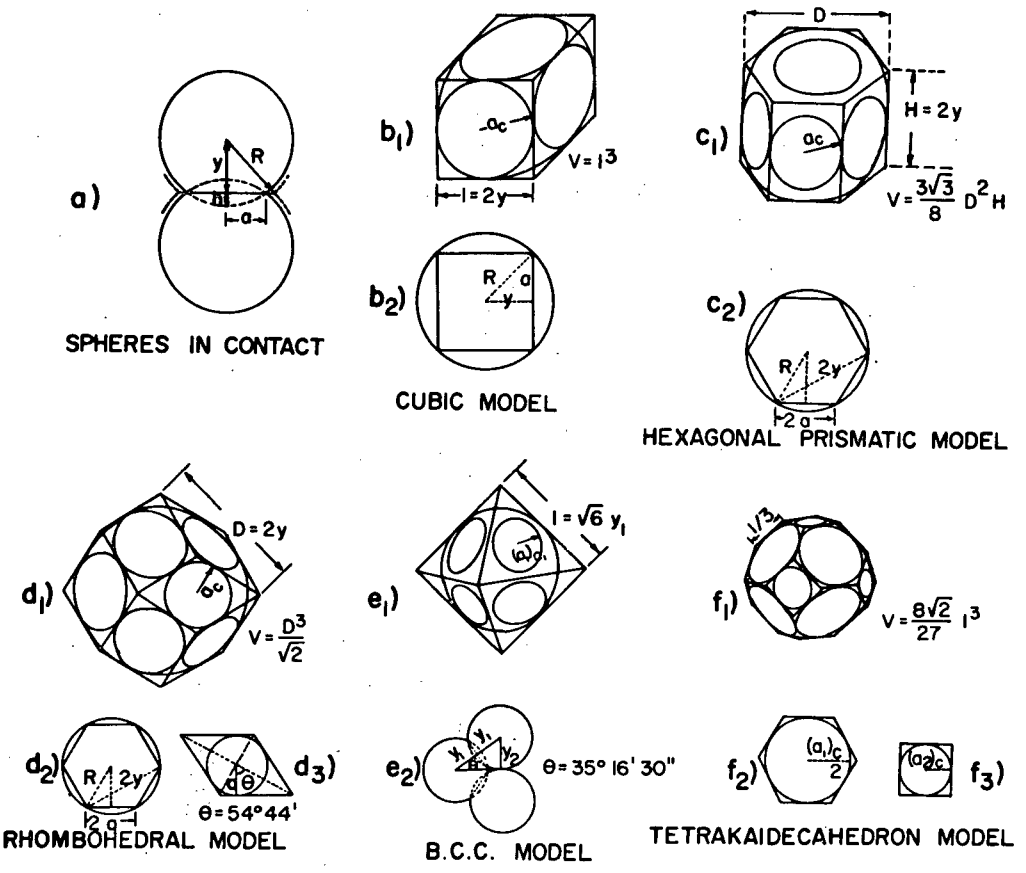

Figure 5. Geometric relationship of different models (After Kakar[13]).

unit cell is composed of the deformed sphere with its associated void space).

II.1.a. Simple Cubic Packing

Consider a cubic array of spheres deformed under hydrostatic pressure. Each sphere will have six flat faces formed as shown in Figures $5b_1$ and $5b_2$. The unit cell in this case is a cube of side 2y where $y = (R^2-a^2)^{1/2}$.

The cross-sectional area of the unit cell is $4y^2$. If there is a load 'ℓ' on each face, then the stress on each face is $\ell/4y^2$ and the total pressure acting on each sphere is $\frac{6\ell}{4y^2}$. This has to be equal to the total load on the system under hydrostatic conditions. In conventional hot-pressing generally a unidirectional load is applied, but because of the existence of back stress from the die-wall and other plunger, the stress at the central core of a die is approximately isotropic. This was experimentally observed by Kakar,[13] while measuring the contact face radii of hot-pressed lead spheres.

The load acting on each face of the unit cell can be divided into two components; one part acting on the sphere through its indented flat face and the other part on the void space, i.e.

$$4y^2\sigma = \pi a^2\sigma_1 + c\sigma_2 \qquad (6)$$

where σ_1 is the stress on the neck, σ_2 is the stress on the void space (= 0), σ is the applied stress, c is the cross-section area of porosity and a is the radius of the neck.

$$\sigma_1 = \frac{4y^2}{\pi a^2}\,\sigma$$

or

$$\sigma_1 = \frac{4}{\pi}\,\frac{(R^2-a^2)}{a^2}\,\sigma \tag{7}$$

From equation (5)

$$D = \frac{1}{\beta(R^2-a^2)^{3/2}}$$

where $\beta = 8$ for the simple cubic packing and this equation can be rewritten as

$$D^{2/3}\beta^{2/3}R^2-1 = \frac{a^2}{R^2-a^2} \tag{8}$$

Substituting equation (8) in equation (7)

$$\sigma_1 = \frac{4}{\pi}\,\frac{1}{(D^{2/3}\beta^{2/3}R^2-1)}\,\sigma \tag{9}$$

Substituting equation (9) in equation (3)

$$\dot{\varepsilon} = A\left\{\frac{1}{\pi/4}\,\frac{\sigma}{(D^{2/3}\beta^{2/3}R^2-1)}\right\}^n \tag{10}$$

Combining equations (10) and (4)

$$\frac{1}{D}\frac{dD}{dt} = A\left\{\frac{1}{\pi/4}\,\frac{\sigma}{(D^{2/3}\beta^{2/3}R^2-1)}\right\}^n \tag{11}$$

This on integration yields

$$\int_{D_o}^{D_{max}} D^{-1}\{D^{2/3}\beta^{2/3}R^2-1\}^n \, dD = \int_o^t A\left(\frac{\sigma}{\pi/4}\right)^n dt \qquad (12)$$

II.1.b. Orthorhombic Packing

Each sphere after deformation will have eight faces. The model for the deformed sphere and the unit cell are shown in Figures $5c_1$ and $5c_2$. The cross-sectional area of the unit cell is $2\sqrt{3}\, y^2$ where $y = (R^2-a^2)^{1/2}$. Computing the load for the top face of the unit cell,

$$2\sqrt{3}\, y^2\sigma = \pi a^2\sigma_1 + c\sigma_2 \qquad (13)$$

σ = applied stress

σ_1 = stress on the neck

σ_2 = stress on porosity = 0

$$\sigma_1 = \frac{2\sqrt{3}}{\pi}\,\frac{y^2}{a^2}\,\sigma \qquad (14)$$

or

$$\sigma_1 = \frac{2\sqrt{3}}{\pi}\,\frac{R^2-a^2}{a^2}\,\sigma \qquad (15)$$

Substituting equation (8) in equation (15)

$$\sigma_1 = \frac{1}{\pi/2\sqrt{3}}\,\frac{\sigma}{[D^{2/3}\beta^{2/3}R^2-1]} \qquad (16)$$

where $\beta = 4\sqrt{3}$ for the orthorhombic packing.

Combining equations (3), (4) and (16)

$$\frac{1}{D}\frac{dD}{dt} = A\left\{\frac{1}{\pi/2\sqrt{3}}\ \frac{\sigma}{(D^{2/3}\beta^{2/3}R^2-1)}\right\}^n \tag{17}$$

The integral form of equation (17) is

$$\int_{D_o}^{D_{max}} D^{-1}\{D^{2/3}\beta^{2/3}R^2-1\}^n\, dt = \int_o^t A\left(\frac{\sigma}{\pi/2\sqrt{3}}\right)^n dt \tag{18}$$

II.1.c. Rhombohedral Packing

Each sphere has twelve points of contact and the resultant unit cell is a rhombic dodecahedron as shown in Figures $5d_1$ and $5d_2$.

The cross-sectional area of the unit cell is $2\sqrt{3}\ y^2$ where $y = (R^2-a^2)^{1/2}$. Computing the loads for the top face of the unit cell,

$$2\sqrt{3}\ y^2\sigma = 3\pi a^2\cos\theta\sigma_1 + c\sigma_2 \tag{19}$$

σ = applies stress

σ_1 = stress on the neck

σ_2 = stress on porosity = 0

From geometry $\cos\theta = \sqrt{2/3}$

$$\sigma_1 = \frac{2\sqrt{3}}{\sqrt{6}\pi}\ \frac{y^2}{a^2}\sigma \tag{20}$$

or,

$$\sigma_1 = \frac{2\sqrt{3}}{\sqrt{6}\pi}\ \frac{R^2-a^2}{a^2}\sigma \tag{21}$$

Substituting equation (8) in equation (21)

$$\sigma_1 = \frac{1}{\pi/\sqrt{2}} \frac{\sigma}{[D^{2/3}\beta^{2/3}R^2-1]} \tag{22}$$

where $\beta = 4\sqrt{2}$ for the rhombohedral packing.

Combining equations (3), (4) and (22)

$$\frac{1}{D}\frac{dD}{dt} = A\left\{\frac{1}{\pi/\sqrt{2}} \frac{\sigma}{(D^{2/3}\beta^{2/3}R^2-1)}\right\}^n \tag{23}$$

This, on integration, yields

$$\int_{D_o}^{D_{max}} D^{-1}\{D^{2/3}\beta^{2/3}R^2-1\}^n \, dD = \int_o^t A\left(\frac{\sigma}{\pi/\sqrt{2}}\right)^n dt \tag{24}$$

II.1.d. B.C.C. Packing

The shape of deformed sphere is schematically represented in Figures $5e_1$ and $5e_2$. There are eight points of contact during the initial stage of deformation.

The cross-sectional area of the unit cell is $\frac{16}{3} y^2$ where $y = (R^2-a^2)^{1/2}$.

Computing the loads for the top face of the unit cell

$$\frac{16}{3} y^2\sigma = 4\pi a^2 \cos\theta\sigma_1 + c\sigma_2 \tag{25}$$

σ = applied stress

σ_1 = stress on neck

σ_2 = stress on porosity = 0

From geometry, $\cos\theta = \frac{1}{\sqrt{3}}$

$$\sigma_1 = \frac{16}{3} \frac{\sqrt{3}}{4\pi} \frac{y^2}{a^2} \sigma \tag{26}$$

or

$$\sigma_1 = \frac{4}{\sqrt{3}\pi} \frac{R^2-a^2}{a^2} \sigma \tag{27}$$

Substituting equation (8) in equation (27)

$$\sigma_1 = \frac{1}{\pi\sqrt{3}/4} \frac{\sigma}{[D^{2/3}\beta^{2/3}R^2-1]} \tag{28}$$

Combining equations (3), (4) and (28)

$$\frac{1}{D}\frac{dD}{dt} = A\left\{\frac{1}{\pi\sqrt{3}/4} \frac{\sigma}{(D^{2/3}\beta^{2/3}R^2-1)}\right\}^n \tag{29}$$

This, on integration gives

$$\int_{D_o}^{D_{max}} D^{-1}\{D^{2/3}\beta^{2/3}R^2-1\}^n \, dD = \int_o^t A\left(\frac{\sigma}{\pi\sqrt{3}/4}\right)^n dt \tag{30}$$

II.2 General Equations

From the above, it appears one can write general equations both for the stress concentration factor and for the densification as follows:

$$\sigma_1 = \frac{\sigma}{\alpha_1 (D^{2/3}\beta^{2/3}R^2 - 1)} \tag{31}$$

where α_1 and β are constants which vary with packing geometry, and hence

$$\int_{D_o}^{D_{max}} D^{-1}\{D^{2/3}\beta^{2/3}R^2 - 1\}^n \, dD = \int_o^t A\left(\frac{\sigma}{\alpha_1}\right)^n \, dt \tag{32}$$

It should be noted that the derivation is based on a condition where the stress is hydrostatic in nature. It is also assumed that the strain rate at the points of contact and in the whole system approaches a steady-state condition as soon as a load is applied.

II.3 Application of the Equation

The analytical solution of the above equation in a closed form is not possible. The limits of integration D_{max} have values varying from .835 for the hexagonal prismatic model to 0.995 for the tetrakaidecahedron model. In equation (32) β, and α_1 are geometric constants and they are calculable. The values of these constants are shown in Table III. A and n are material constants and can be determined from steady-state hot-working data. Knowing all the constants, the change of D, the relative density of a compact, as a function of time (t) at a constant temperature

and pressure can be obtained by solving the equation in a computer. The computer programme is given in Appendix 5.

For each of the theoretical deformation models, R changes as deformation proceeds; i.e.,R is a function of D. However, the change in R at various stages of deformation can be calculated from the constant volume equation as described by Kakar[13]. Tables of R vs D are given in Appendix 1.

Table III. Geometric Constants of Different Models

Model	α_1	β	D_o	D_{max}
cubic	$\pi/4$	8	.523	0.965
hexagonal prism	$\pi/2\sqrt{3}$	$4\sqrt{3}$	.604	0.835
rhombic dodecahedron	$\pi/2$	$4\sqrt{2}$	.740	0.964
tetrakaidecahedron	$\pi\sqrt{3}/4$	$\frac{32\sqrt{3}}{9}$	.680	0.995

CHAPTER III

EXPERIMENTAL VERIFICATION OF THEORY

III.1 Material Selection and Theoretical Plots

To compare the compaction data for hot-pressing with that of theoretically predicted behaviour, both metallic and non-metallic materials were chosen. The selection of lead-2% antimony, nickel and alumina for experimental work was based upon the availability of spherical particles for hot-pressing.

As discussed previously, the theoretical equation can only be tested if the values of the material constants A and n for any material are known or, are experimentally determined by hot-working data. The values of these constants for a large number of metallic and non-metallic materials have been reported in the literature. The purities of the metals (spheres of Pb-2% Sb and Ni) used in this investigation are not the same for which the values of A and n are available in the literature. For this reason, the values of A and n for Pb-2% Sb and Ni were determined from steady-state hot-compression experiments in an Instron machine. The details of the experimental procedure are given in a later section. The values of stress and strain rate are shown in Appendix 2. The values of A and n for alumina are obtained from the literature. The value of the constants A and n for all the materials are shown in Table IV.

Using the values from the table and the theoretical equation (equation 32), a series of plots of relative density (D) as a function of time (t) were generated for different temperatures and pressures. These theoretical plots are shown in the following figures.

(a) For lead-2% antimony at 100°C under 1500 psi in Fig. 6, lead-2% antimony at 150°C under 918 psi in Fig. 7.

(b) For nickel at 800°C under 2162 psi in Fig. 8, nickel at 900°C under 2105 psi in Fig. 9.

(c) For alumina at 1600°C under 5000 psi in Fig. 10.

For these plots all four geometric models were employed.

III.2 Experimental Tests and Procedures

III.2.a. Apparatus

(i) Lead-2% antimony: For these hot-pressing experiments 1.5 mm average diameter lead-2% antimony shots were used. This material was supplied by the Lead Shot Industries Limited. The apparatus used for hot-pressing of lead-2% antimony shots is shown in Figure 11. A uniaxial compressive load was applied to the system through a simple bar. A stainless steel (316) rod activated by a lever arm was placed inside a stainless steel tube. The compact was positioned on top of the steel rod in a die and the stress was applied to the specimen between the rod and a plug welded into the centre of the tube. To ensure a uniform stress across the compact a hemispherical plunger and cup were used to transmit the load to the compact. A 400 watt tube furnace with a uniform hot zone 3 inches long was placed around the stainless steel tube. The temperature of the furnace was raised and

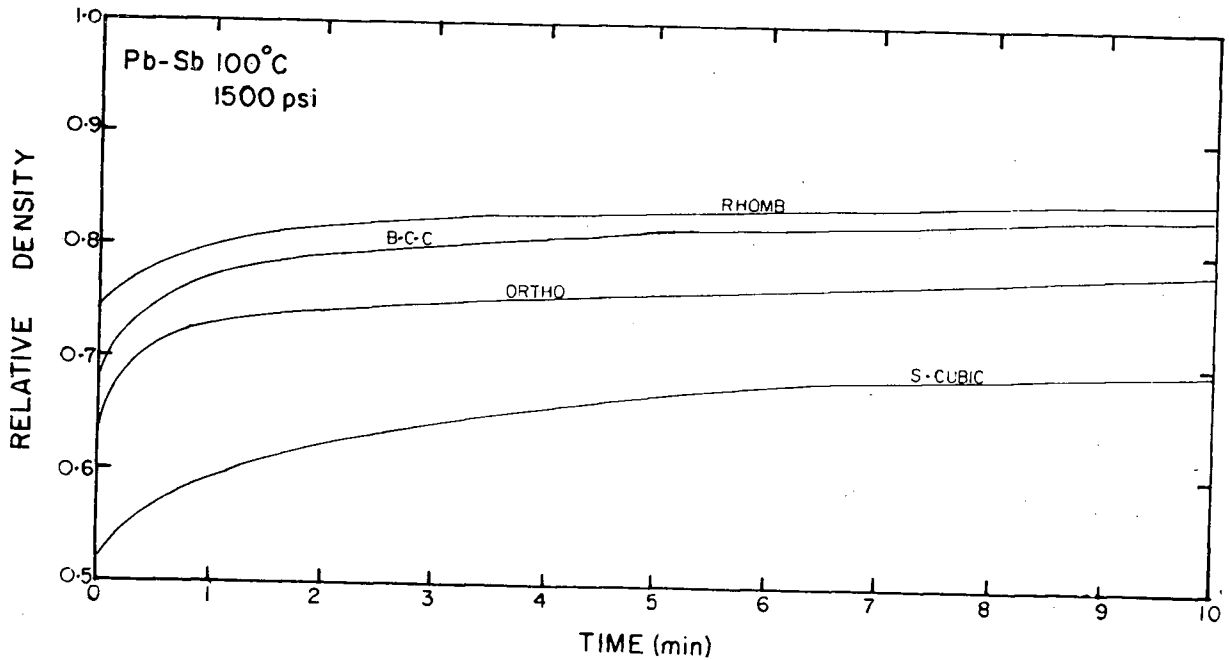

Figure 6. D vs. t plot for Pb-2% Sb at 100°C under 1500 psi (theoretical plots).

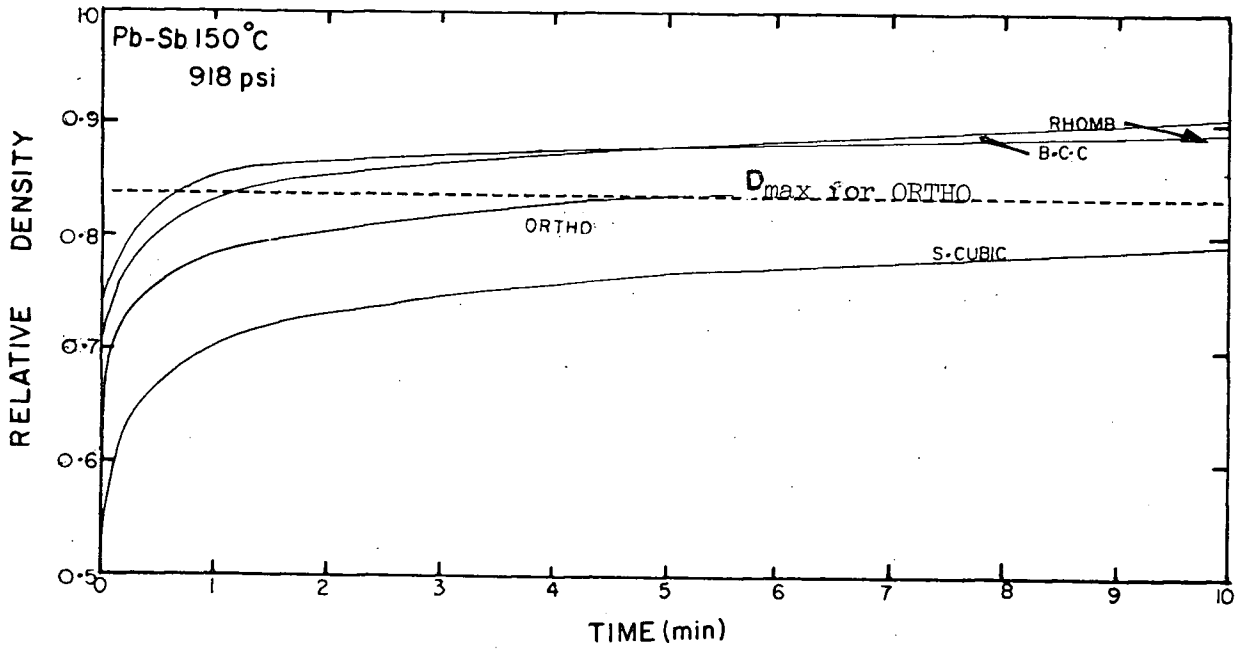

Figure 7. D vs. t plot for Pb-2% Sb at 150°C under 918 psi (theoretical plots).

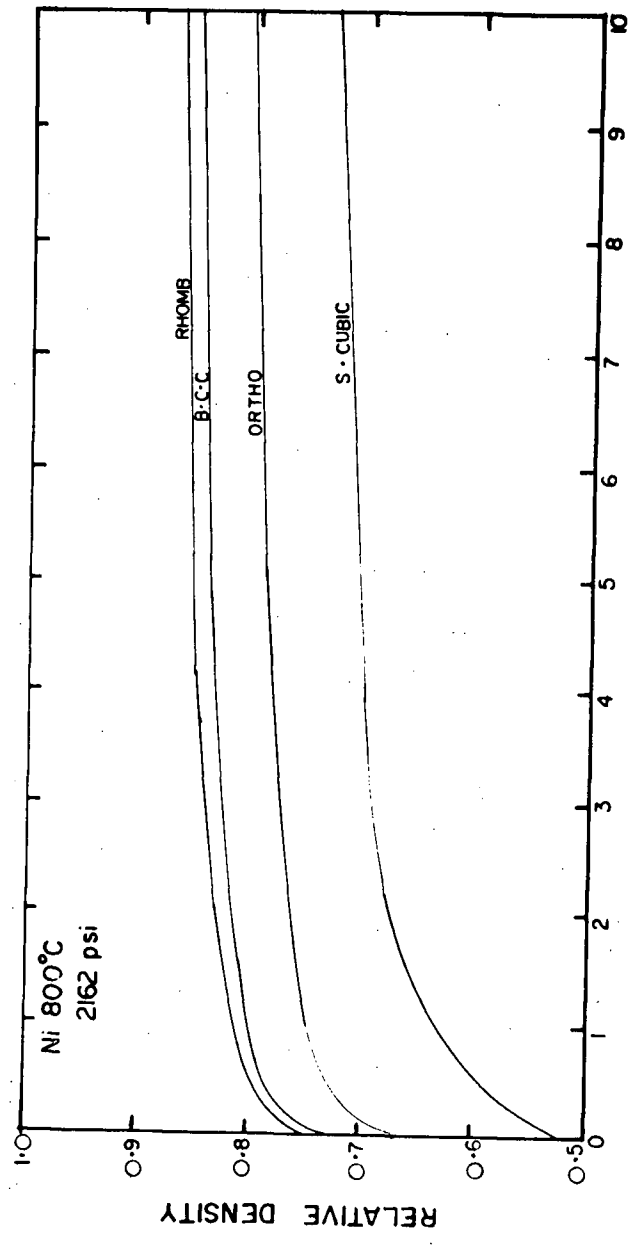

Figure 8. D vs. t plot for Ni at 800°C under 2162 psi (theoretical plots).

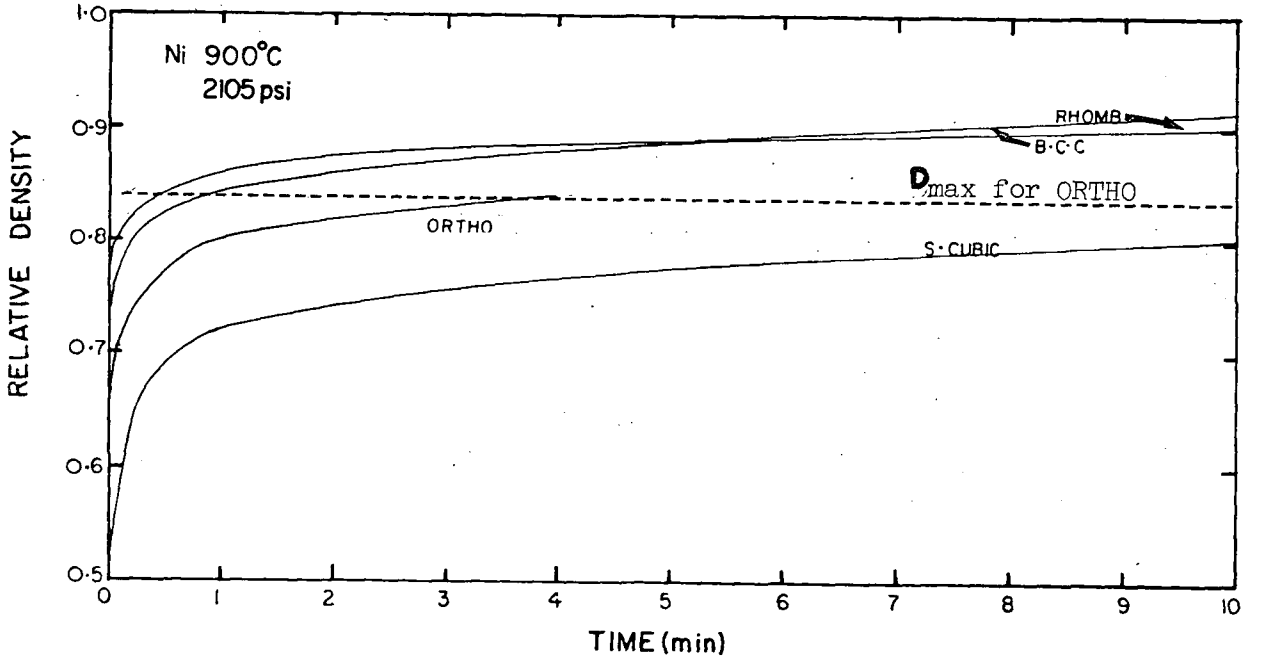

Figure 9. D vs. t plot for Ni at 900°C under 2105 psi (theoretical plots).

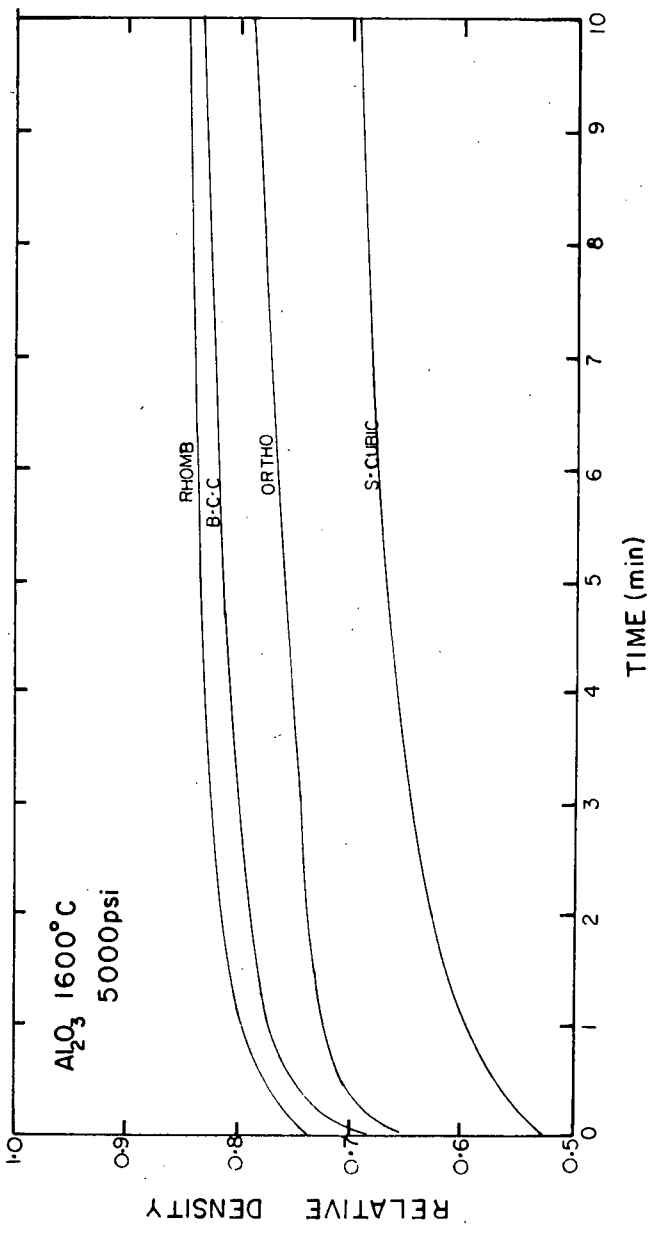

Figure 10. D vs. t plot for Al_2O_3 at 1600°C under 5000 psi (theoretical plots).

Table IV. Material Constants for Different Materials

Materials	Temperature (°C)	A (sec^{-1})	n
Lead-2% antimony	100	4.11×10^{-21}	4.2
	150	3.519×10^{-19}	4.2
Nickel	800	4.6×10^{-23}	4.6
	900	3.4×10^{-22}	4.6
Alumina	1600	2.0×10^{-22} †	4.0†

† Values obtained from Warshaw et al.[27]

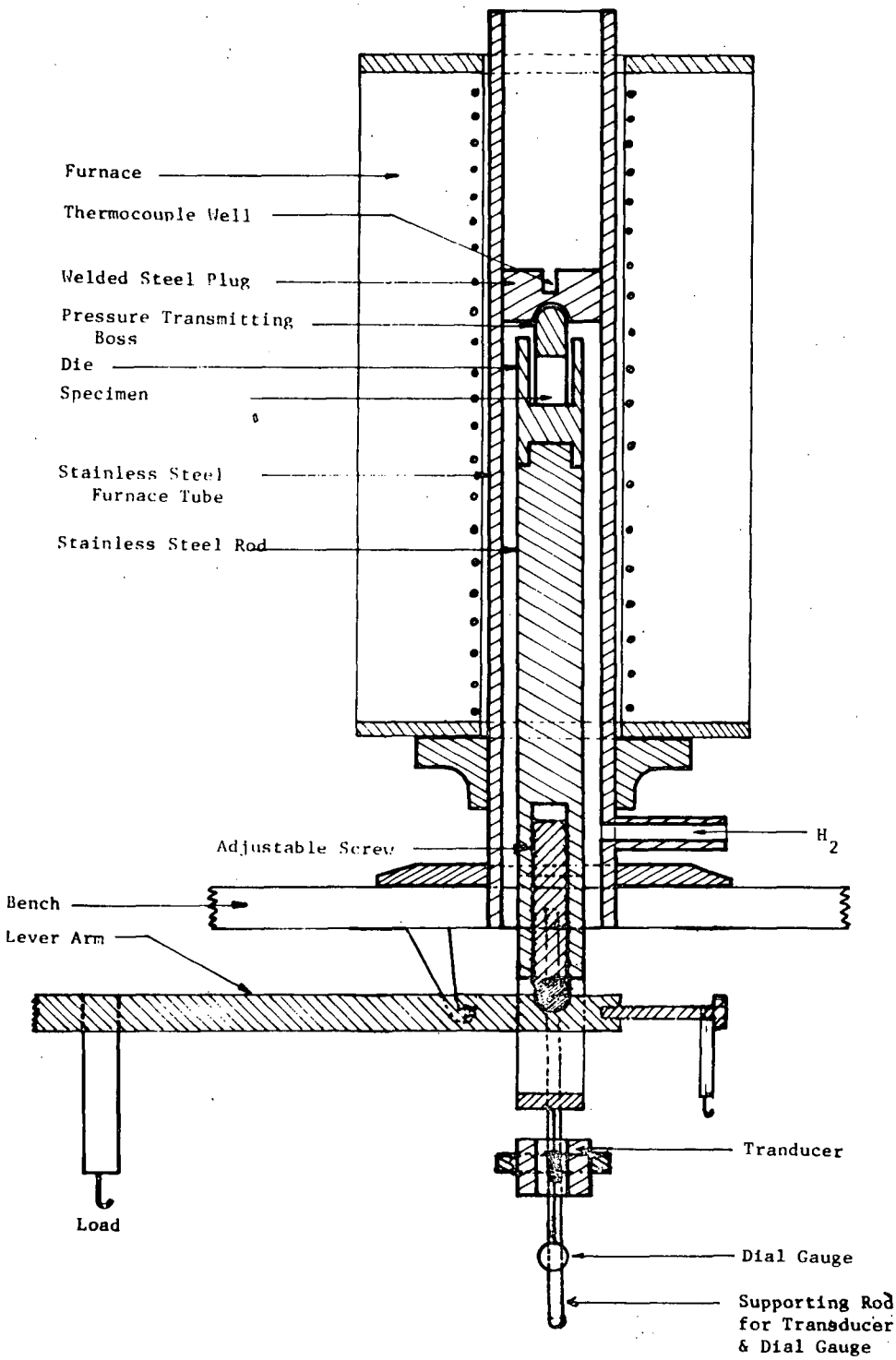

Figure 11. Hot-pressing apparatus used for Pb-2% Sb shots.

maintained at the desired temperature. A chromel-alumel thermocouple situated 1/2 inch from the specimen operated a proportional temperature controller which maintained the specimen temperature within $\pm$ 5°C.

The compaction was determined by the displacement of the extension of the stainless steel rod, which was obtained by the output from an electromagnetic transducer attached to the extension rod. The transducer output was analysed by a Phillips PR 19300, direct reading bridge which was connected to a "Heath Kit" Servo Recorder.

The loading system was calibrated by hanging weights at the point of contact of the bar and the stainless steel rod. The load was very close to the product of the weight on the bar and the ratio of the arms. The weight of the bar was compensated for by loading a small weight at the other end.

III.2.a.ii Nickel (99% Ni and 0.7% Co): For hot-pressing of nickel, 0.65 mm average diameter nickel balls were used. These were supplied by the Sherritt Gordon Mines Limited, Fort Saskatchewan, Alberta. The hot-pressing was carried out in a molybdenum die with an external graphite sleeve, using induction heating. Both the die and graphite sleeve acted as susceptors. The experimental set up is shown in Figure 12. The temperature of the compact was recorded through the top plunger at a distance 1/6 inch from the specimen and was controlled by the same thermocouple. A Pt-Pt-10% Rh thermocouple was used. The measurement of the displacment of the moveable bottom ram (the top ram with the thermocouple was rigidly attached to the press) was obtained by the output from an electromagnetic transducer attached to the ram. The transducer output was analysed by a Phillips direct reading measuring

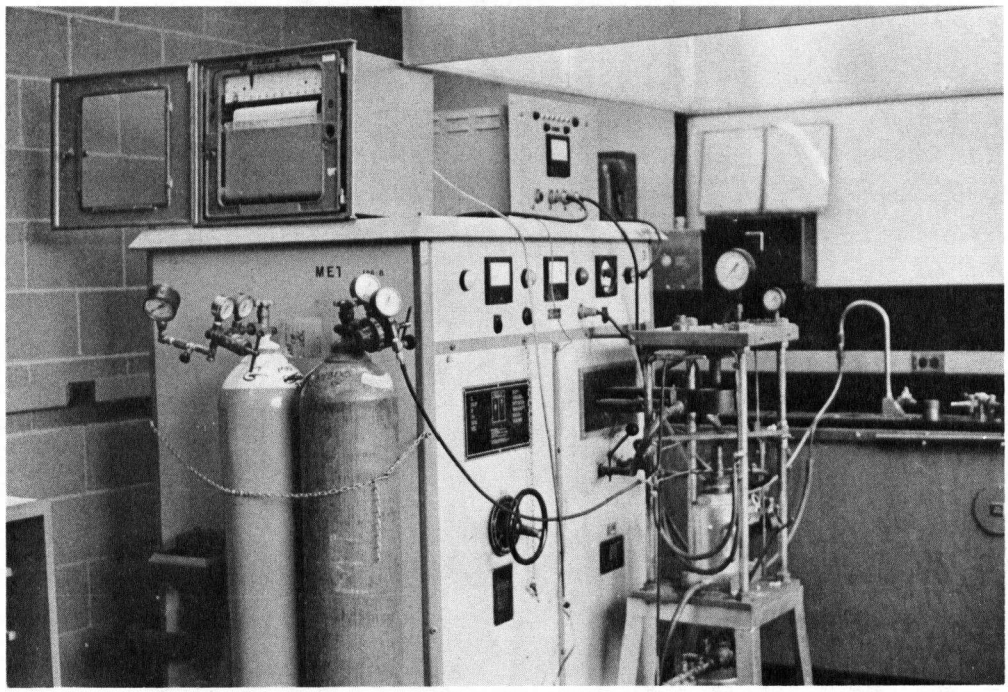

Figure 12. Hot-pressing apparatus used for Ni and Al_2O_3 spheres.

bridge, which was connected to a "Heath Kit" servo-recorder, as used previously for the compaction experiments with lead-2% antimony spheres.

(iii) Alumina: The same apparatus (hot-pressing induction unit) which was used for nickel experiments was also used for the compaction studies of alumina. In this case, however, a graphite die was used instead of a molybdenum die-graphite sleeve combination as used previously. 1 mm sapphire spheres were used in this case and these were supplied by A. Miller and Company, Libertyville, Illinois.

III.2.b. Procedures

(i) Hot-pressing: A weighed amount of spheres was poured into a die, tapped and well-shaken in order to obtain uniform packing and maximum density. The initial height of the die with plungers was measured and subsequently the height of die, with plungers and specimen, before hot-pressing was also measured. This gave the initial height of the specimen. It took 15-20 minutes for the specimen to reach the furnace temperature after the die assembly was introduced in the furnace. During this heating up period, the plunger displacement recording system was connected. No appreciable shrinkage or expansion was recorded during the heating up period. Once the specimen attained the equilibrium temperature the pre-weighed load was placed on the lever arm for lead. In the case of nickel and alumina the load was applied through a hydraulic jack, which activated the press. The press was calibrated by an Instron machine using an 'F' cell. The calibration curve is shown in Figure 13.

A hydrogen atmosphere was used during hot-pressing of lead-2% antimony

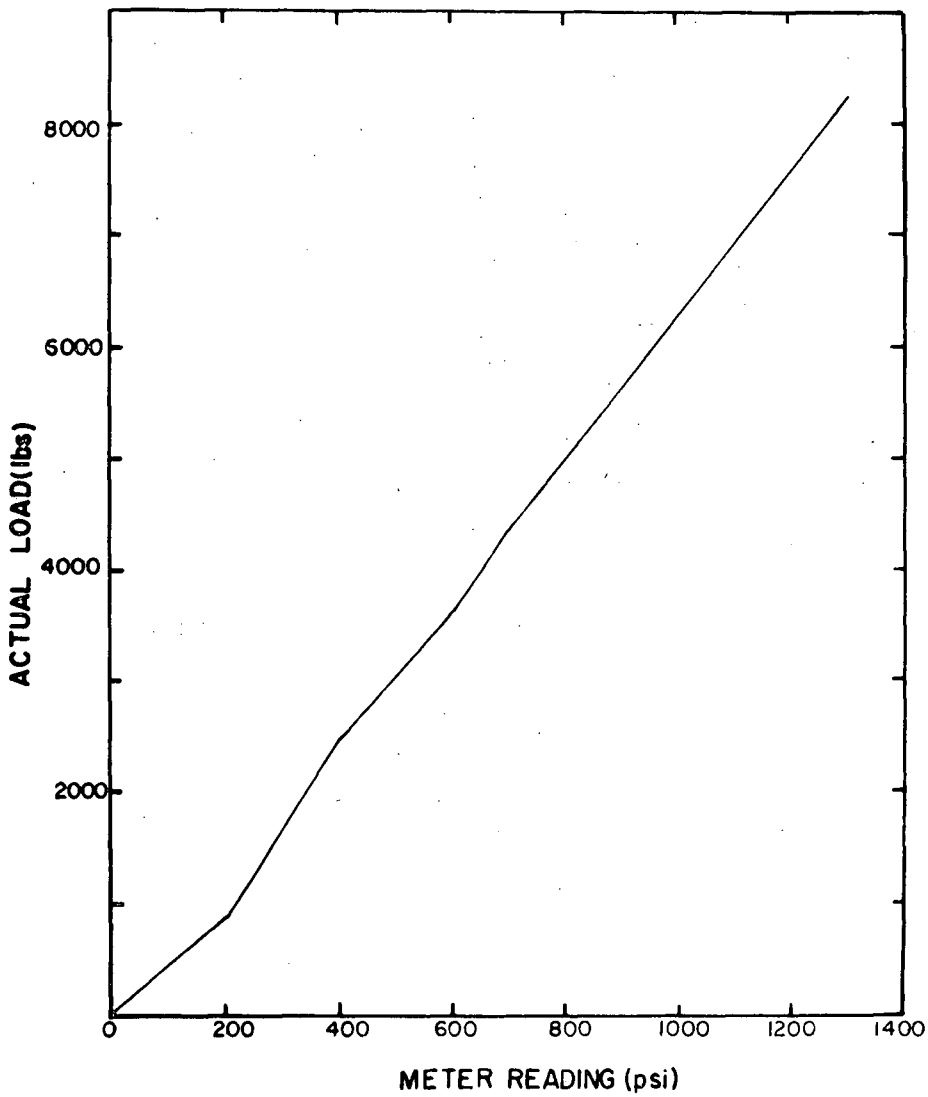

Figure 13. Calibration curve for the pressure-gauge used for hot-pressing of Ni and Al_2O_3.

and nitrogen was used in the case of nickel and alumina. After the application of pressure, the shrinkage was recorded as a function of time. When the compaction rate was drastically reduced and the compaction curve had levelled off, the power to the furnace was shut off and the specimen was cooled in the furnace. The height of the specimen in the die with plungers after hot-pressing was measured. The experimental test conditions used during hot-pressing are shown in Table V.

The volume of the compact was calculated before and after hot-pressing using the height of the compact and the diameter of the die, which remained constant. The weight of the compact was known and also remained constant. From these measurements the initial and final bulk-densities were calculated. From the recorder chart the compact height at any instant during compaction could be found. Using these charts, the change in bulk-density as a function of time under isothermal conditions was obtained. Afterwards the values of the bulk density were converted into relative density by dividing these values by the theoretical density of the solid.

III.2.b.ii Hot-compression of lead-2% antimony and nickel

1. Lead-2% antimony: The Pb-2% Sb shots were melted and cast in the form of small ingots (0.5 x 0.5 x 3 inches). Specimens were cut from these ingots with a jewellers saw, the majority of dimensions were 0.2 x 0.2 x 1 inch. The specimens were annealed at 100°C for 5-6 hours. Prior to testing, the ends of each specimen were ground perpendicular to the longitudinal axis. All specimens were tested in a furnace attached to an Instron tensile testing machine under conditions of constant strain

Table V. Test Conditions for Hot-Pressing

Material	Sphere diameter in mm	Temperature in °C	Pressure in psi	Atmosphere
Lead-2% antimony	1.5	100	918,1010,1285	hydrogen
	1.5	150	918,1010	hydrogen
Nickel	0.65	800	2162,3208	nitrogen
	0.65	900	1477,2105	nitrogen
Alumina	1.0	1600	3200,4000	nitrogen

rates. For testing, the specimens were placed upright between alumina buttons (0.7" dia., 0.2" thickness). When the load attained a constant value the test was stopped. From this load and the cross-sectional area of the specimen, the stress was calculated. The experiments were done at 100 and 150°C and at strain rates of 0.002, 0.005, 0.01 and 0.02 in/min. These results are shown in Appendix 2.

2. Nickel: Nickel balls were melted by induction heating and cast in the form of small ingots (0.5" dia., 3" length). Cylindrical specimens (0.25" dia., 0.9" length) were prepared by turning these ingots on a lathe. The specimens were annealed at 1000°C for 5 hours. The ends of each specimen were ground perpendicular to the longitudinal axis. Experiments were conducted at 800 and 900°C and 0.002, 0.005, 0.01, and 0.02 in/min strain rates. These results are shown in Appendix 2.

CHAPTER IV

RESULTS

IV.1 Metals

IV.1.a. Lead-2% Antimony

(i) Relative Density (D) vs. Time (t)

Initial experiments with Pb-2% Sb were made to test which of the four different geometrical models fitted the experimental data. For this, hot-pressing was done at 150°C under 918 psi and compaction curve was obtained. Both theoretical plots and the experimental data are shown in Figure 14. It is apparent from the figure that the data coincided with the orthorhombic model in the later stages of hot-pressing, with a deviation at an early stage of compaction. The same observation was made for nickel compacts at 800°C and 900°C under 2162 psi and 2105 psi pressures respectively, as shown in Figures 15 and 16.

An overall comparison of compaction data with the theoretical curves indicated that the experimental data followed closely the theoretically predicted curves for the orthorhombic model. For this reason all the theoretical plots in subsequent figures were computed with geometric constants for the orthorhombic model only. The reason for this agreement between the data and the curves for the orthorhombic model is discussed in a later section. In some cases, the experimental compaction data obtained were beyond the upper limit of the density, predicted by the theoretical orthorhombic model. However, these data were excluded from the figures, as the theory of compaction is not valid over .835 relative density.

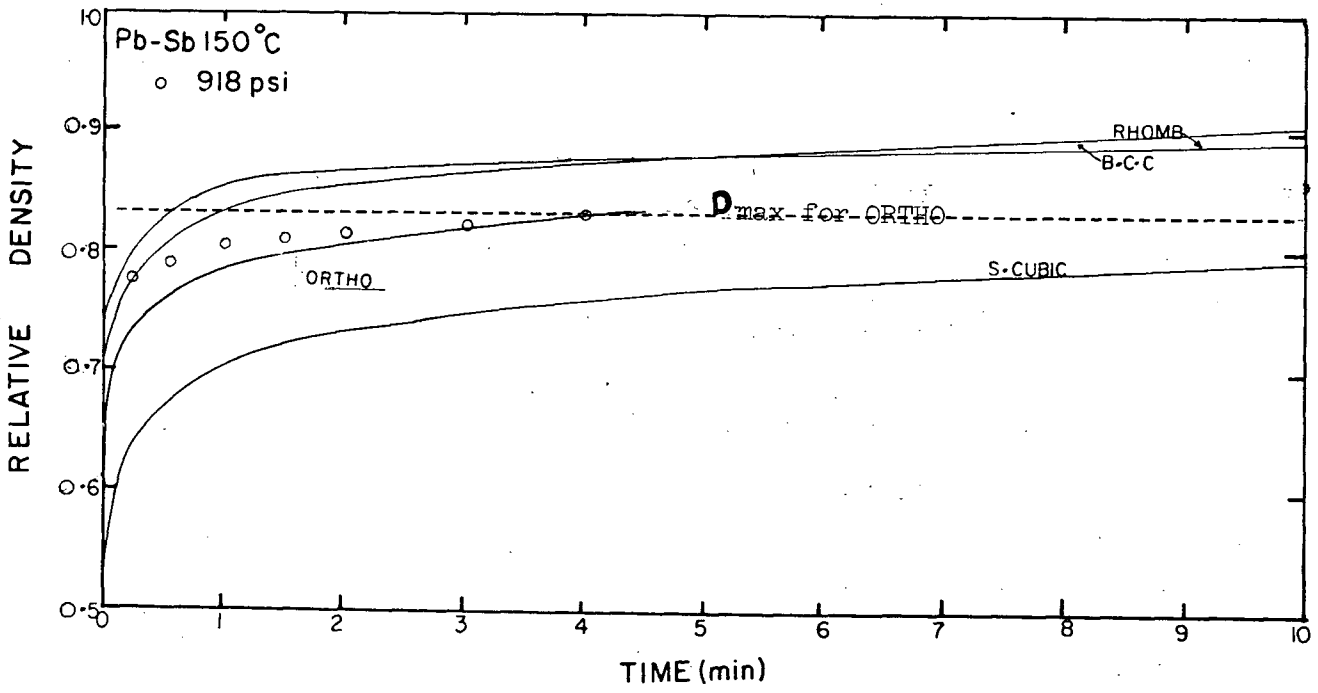

Figure 14. D vs. t plot for Pb-2% Sb at 150°C under 918 psi (solid lines represent the theoretical curves for 4 different models).

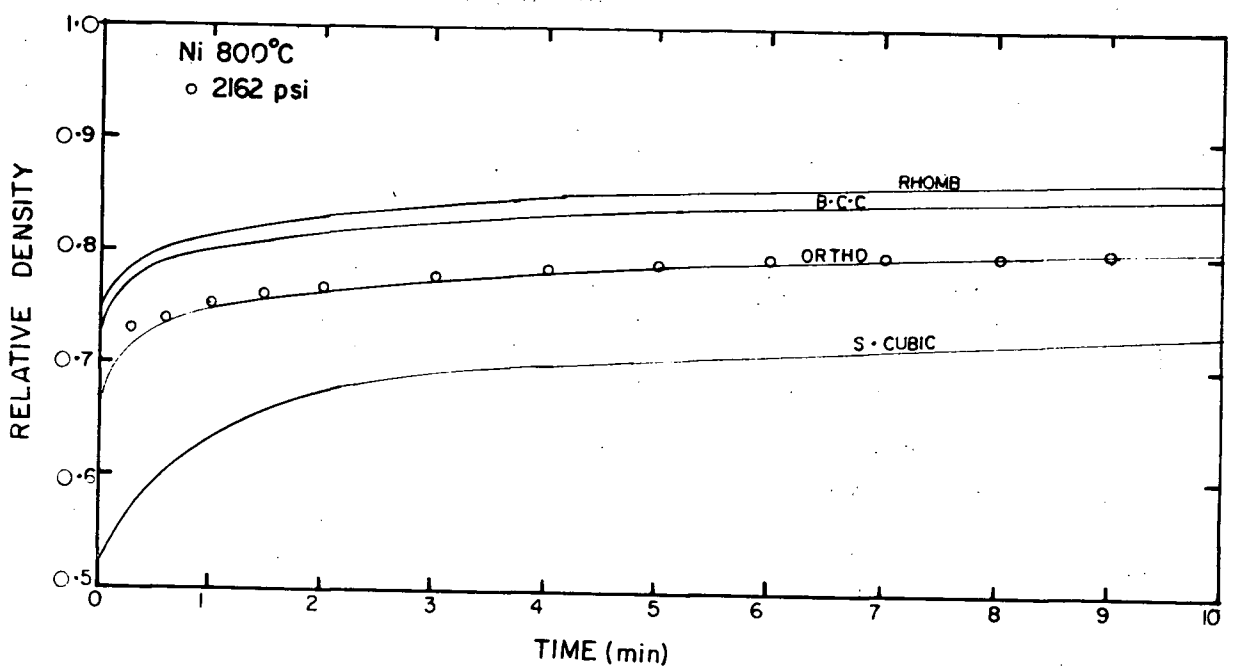

Figure 15. D vs. t plot for Ni at 800°C under 2162 psi (solid lines represent the theoretical curves for 4 different models).

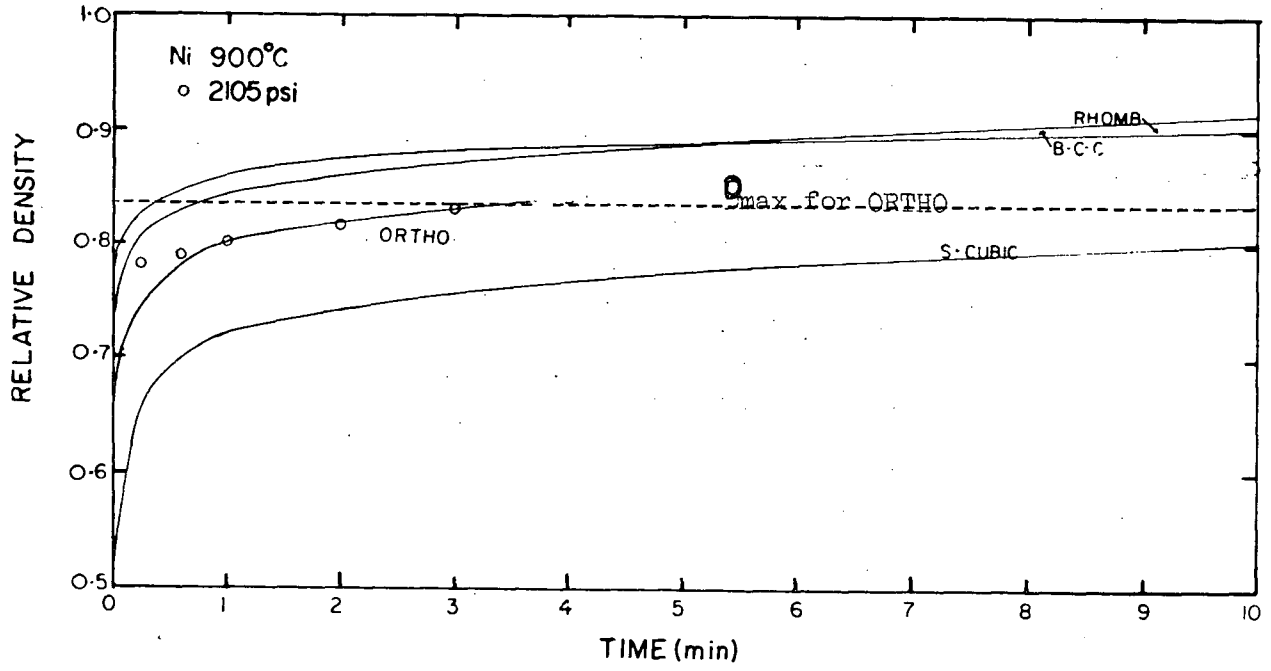

Figure 16. D vs. t plot for Ni at 900°C under 2105 psi (solid lines represent the theoretical curves for 4 different models).

(ii) D vs. t at a constant temperature and under varying pressures: For this, hot-pressing experiments were carried out at 100 (3 stresses) and 150°C (2 stresses) under 918, 1010 and 1285 psi. A series of theoretical curves for the orthorhombic model only were obtained from the computer. The experimental data and the theoretical curves are shown in Figures 17a and 17b. A good fit of experimental points with the theoretical plots can be seen particularly at the later stages of compaction.

(iii) D vs. t at a constant stress and with varying temperatures: For this, experiments were made at 100° and 150°C at a stress of 918 psi. In addition, other experiments were also carried out at 100 and 150°C under 1010 psi stress. The experimental data and the theoretical plots are compared in Figures 18a and 18b for these two sets of experiments. Again a good fit is apparent between experimental points and the theoretical prediction.

IV.1.b. Nickel

(i) D vs. t at a constant temperature and varying pressures: The experimental conditions used to follow the change of relative density as a function of time for nickel are 800°C at 2162 and 3208 psi. The experimental compaction data and the theoretical plot using equation (32) are compared in Figure 19. Another set of hot-pressing experiments were carried out at 900°C under pressures of 1477 and 2105 psi. These results and the corresponding theoretical plots are shown in Figure 20.

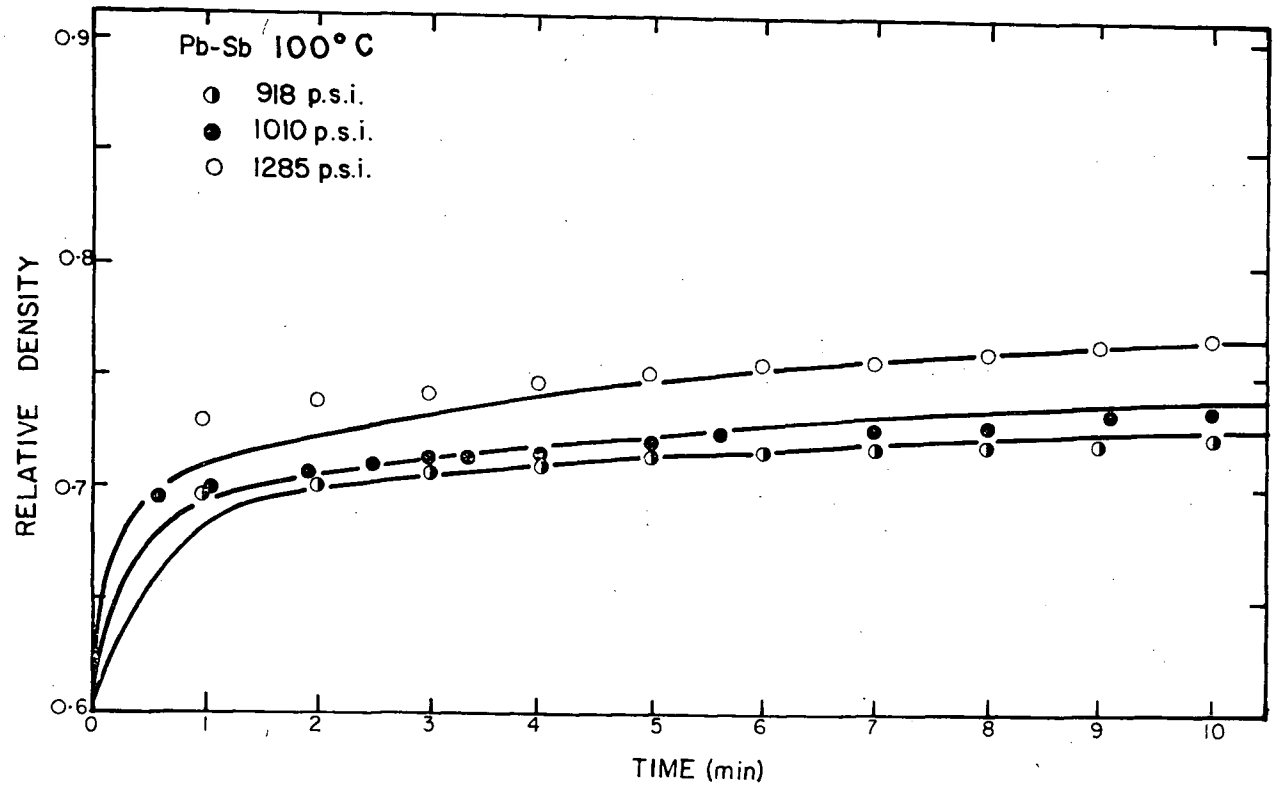

Figure 17(a). D vs. t plot for Pb-2% Sb at 100°C under different pressures (solid line represents the theoretical curve for the orthorhombic model only).

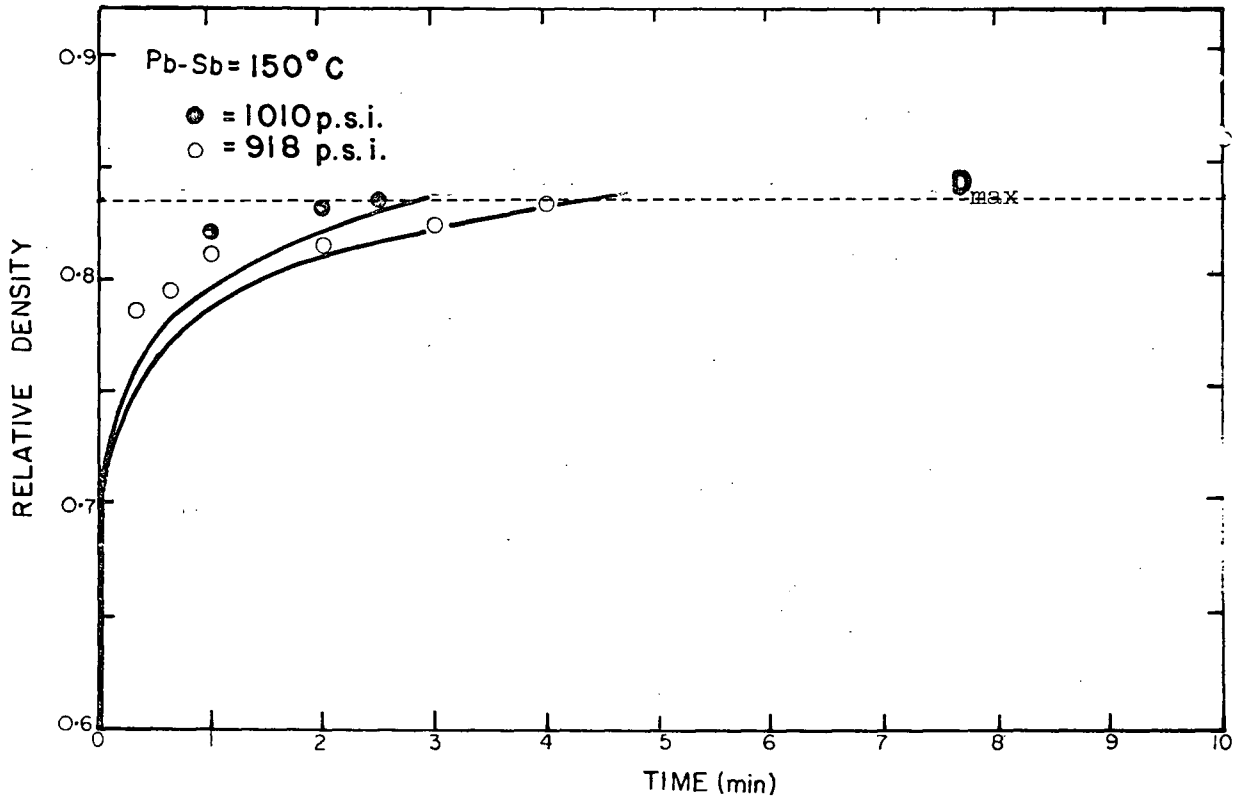

Figure 17(b). D vs. t plot for Pb-2% Sb at 150°C under different pressures (solid line represents the theoretical curve for the orthorhombic model only).

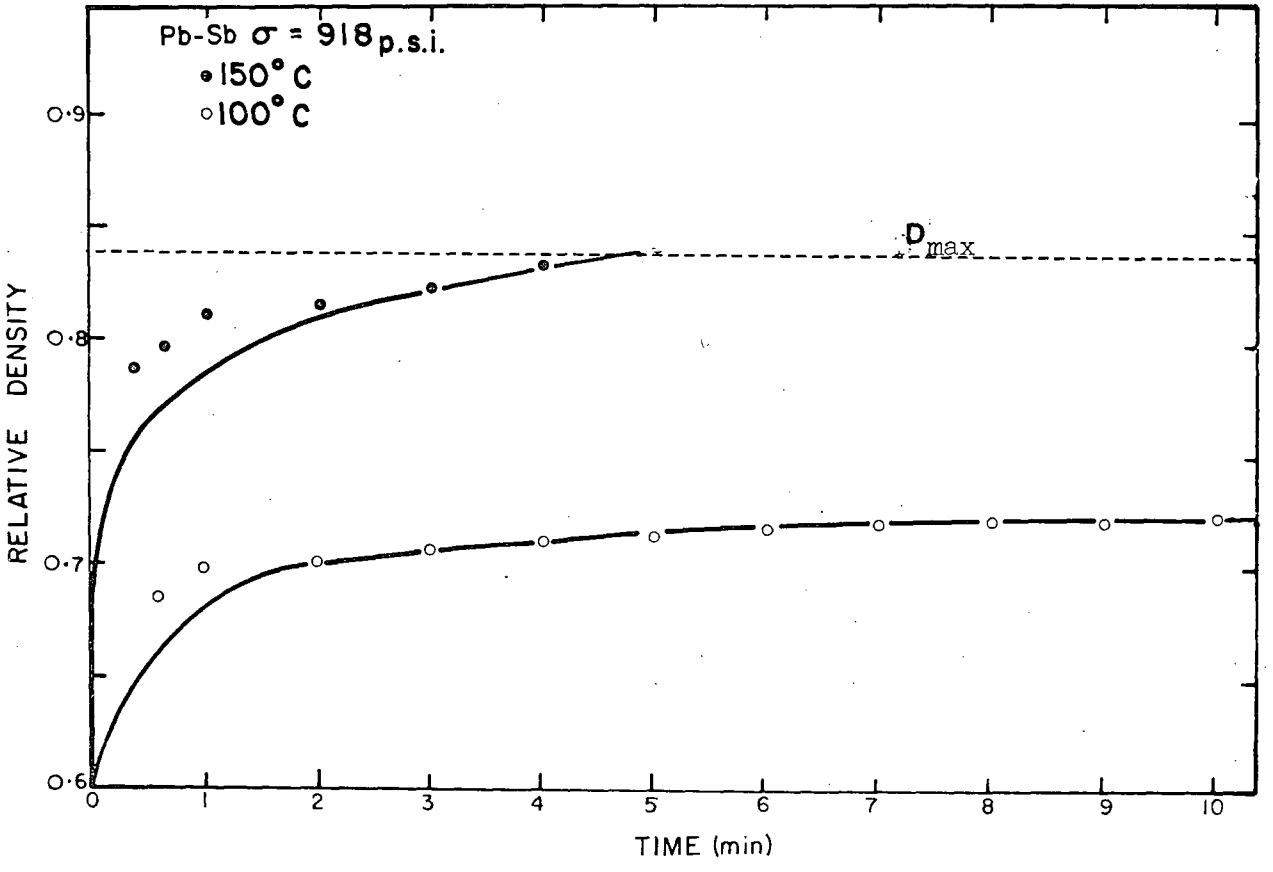

Figure 18(a). D vs. t plot for Pb-2% Sb at 918 psi and different temperatures (solid lines represents the theoretical curve for the orthorhombic model only).

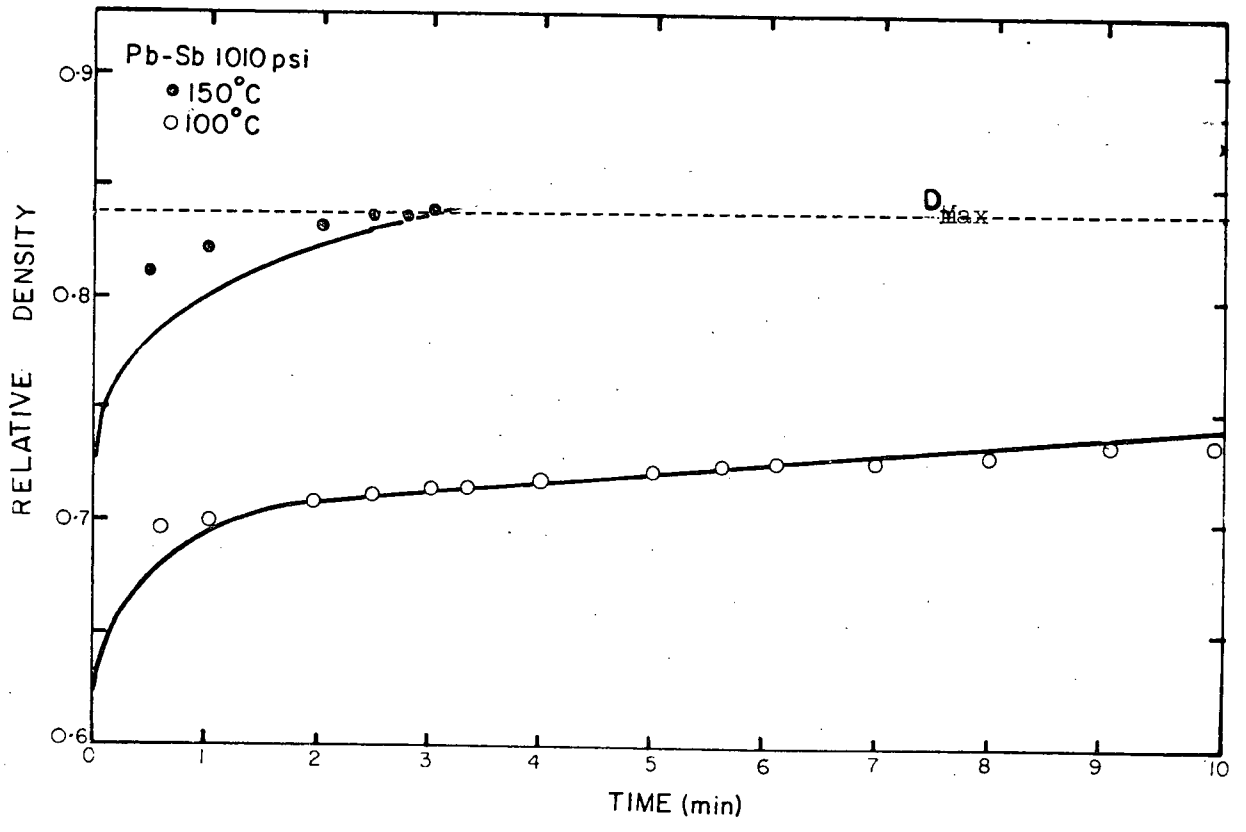

Figure 18(b). D vs. t plot for Pb-2% Sb at 1010 psi and different temperatures (solid line represents the theoretical curve for the orthorhombic model only).

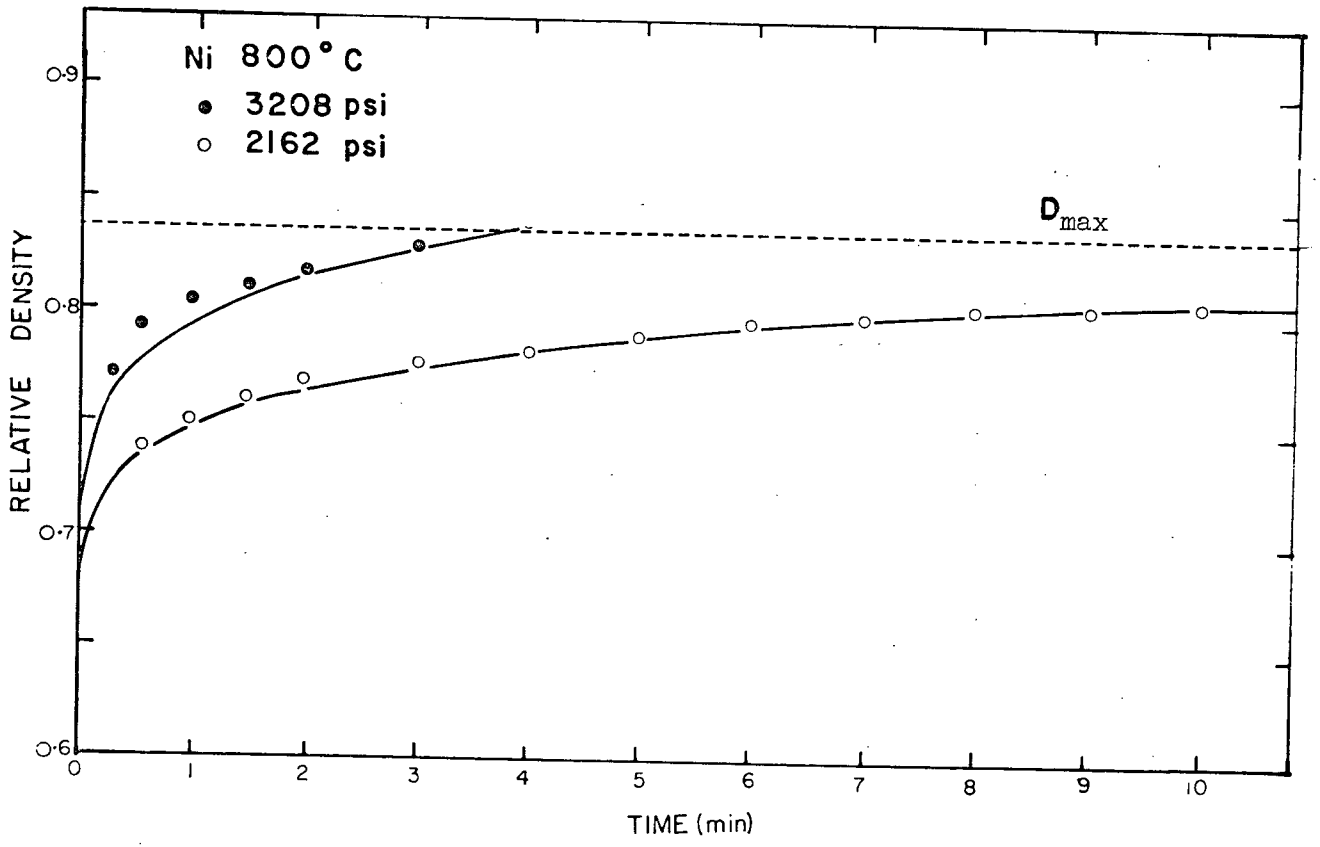

Figure 19. D vs. t plot for Ni at 800°C under different pressures (solid line represents the theoretical curve for the orthorhombic model only).

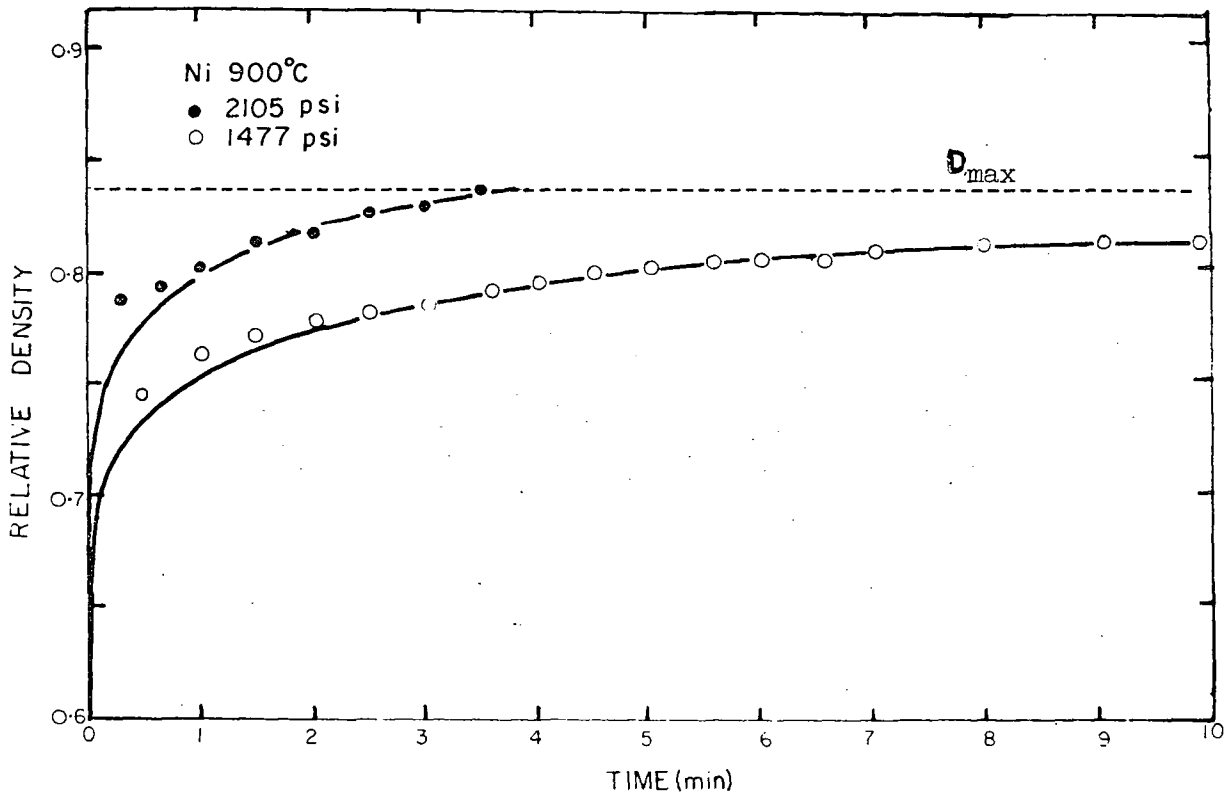

Figure 20. D vs. t plot for Ni at 900°C under different pressures (solid line represents the theoretical curve for the orthorhombic model only).

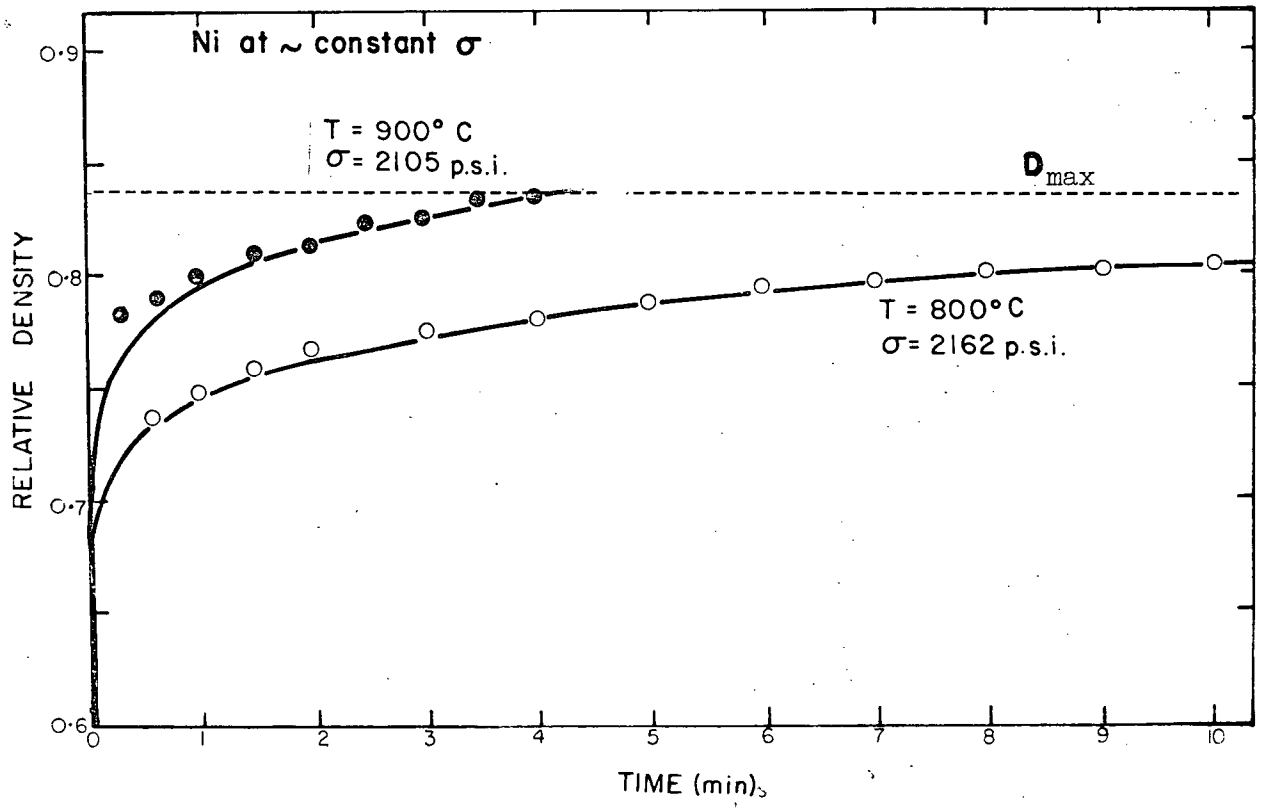

Figure 21. D vs. t plot for Ni at ~ constant stress and different temperatures (solid line represents the theoretical curve for the orthorhombic model only).

(ii) D vs. t at a constant pressure and varying temperatures: To study the effect of changing the temperature at a constant stress on the compaction behaviour of nickel spheres, the curves in Figure 19 and 20 for the conditions 2105 psi at 900°C and 2165 psi at 800°C are replotted in Figure 21. It shows that an increase in temperature of hot-pressing by 100°C shifts the relative density curve by about 10%.

IV.2. Non-Metal

IV.2.a. Alumina

(i) D vs. t at a constant temperature and varying stresses: As only very few alumina spheres (single crystal sapphire spheres) were available for the hot-compaction studies, experiments were done at one temperature (1600°C) and at two different stresses (3200 and 4000 psi). The theoretical curves for D vs. t were also generated under these experimental conditions using equation (32). The experimental data and the theoretical plots are shown in Figure 22. In this case a good fit between the experimental points and the theoretical prediction can be seen during the intermediate stage of hot-pressing. A deviation between the theoretical prediction and experimental results at the very eary stage and during the last stage of compaction was encountered.

IV.3. Strain-Rates During Hot-Pressing

For the calculation of strain-rates from the hot-pressing data, the following equation was used

$$\dot{\varepsilon} = \frac{1}{D}\frac{dD}{dt}$$

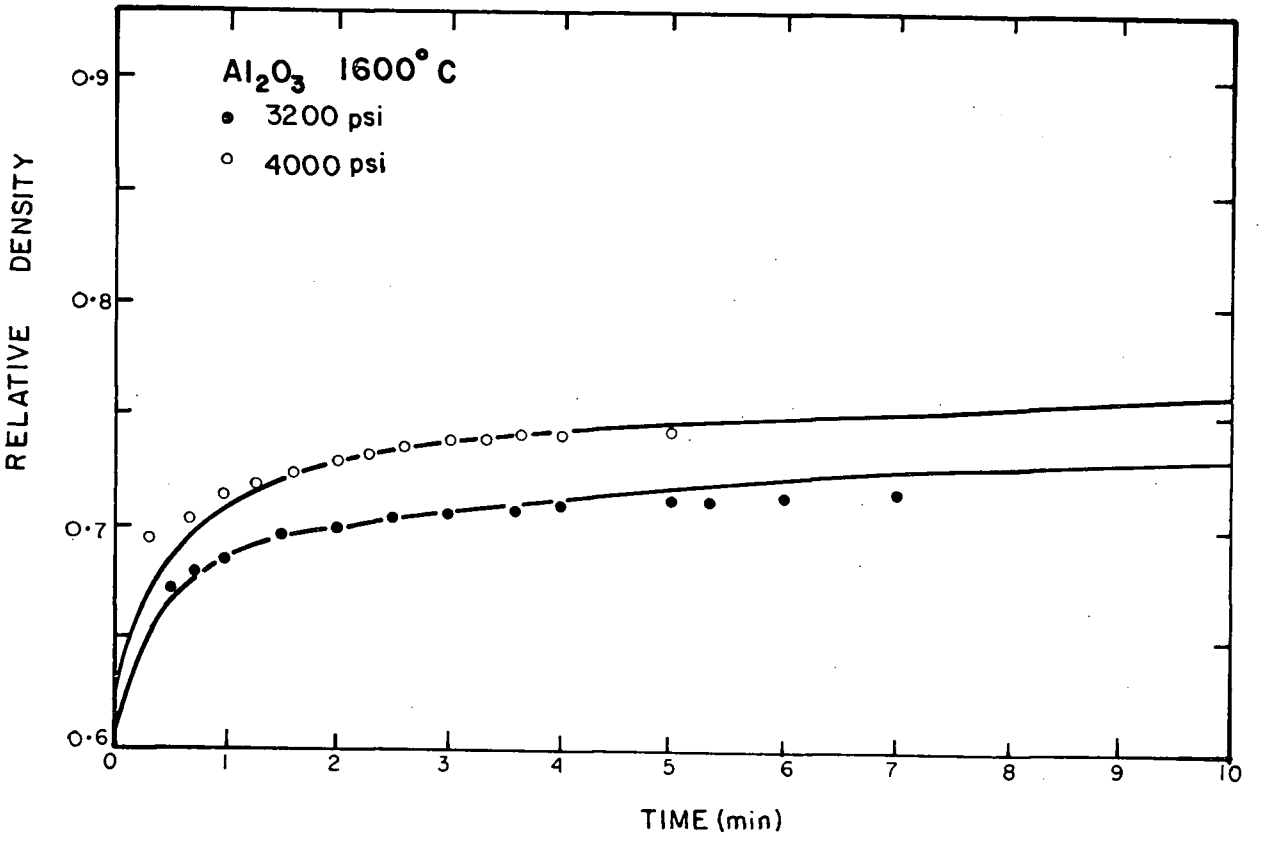

Figure 22. D vs. t plot for Al_2O_3 at 1600°C under different pressures (solid line represents the theoretical curve for the orthorhombic model only).

From the knowledge of the relative density at any stage of compaction and from the slope of the curve D vs. t at that point, the values of strain-rates were calculated and these were tabulated in Appendix 4. It can be seen that the strain rates used for hot compression experiments of Pb-2% Sb and Ni are similar to the values of strain rates at the intermediate stage of densification, although at the initial stage of densification, the strain rates were very much higher than that used for hot-working experiments. It is also at the initial stage, a deviation between the experimental data and the theoretical plots was encountered.

CHAPTER V

DISCUSSION

V.1. Effective Stress During Hot-Pressing

Since the first theoretical work of Murray, Livey and Williams,[19] on the plastic flow theory of hot-pressing, the proponents of stress-enhanced diffusional creep (the Nabarro-Herring creep[20]) have contended that any contribution by plastic flow to the overall densification must be small since the stress on the system during hot-pressing is generally low. It has been recognized lately by most workers, that the effective stress in hot-pressing is different from the applied pressure and that this is a function of porosity. McClelland,[17] the first person to recognise this and to take into account porosity, introduced the following form of effective stress

$$\sigma_{eff} = \frac{P_a}{1-V_p^{2/3}}$$

where P_a is the applied pressure and V_p is the volume fraction porosity. Another form of effective stress was introduced by Vasilos et al.[26] for applying to crystalline materials.

$$\sigma_{eff} = P_a (1 + 2V_p)$$

This was adopted from the change of elastic modulus with porosity as predicte theoretically and observed experimentally. Rossi and Fulrath[21] generalised the form used by Vasilos et al.[26] as follows

$$\sigma_{eff} = P_a(1 + b\ V_p)$$

where b is an empirical constant ($\simeq 2$).

Subsequently a large number of workers (Fairnsworth and Coble,[5], Coble,[3] Fryer,[7] and Koval'Chenko and Samsonov[14]) used the following form of effective stress equation

$$\sigma_{eff} = \frac{P_a}{D}$$

where D is the relative density.

Some of these relations are plotted in Figure 23. It can be seen from this figure that the maximum effective stress is no more than a factor of two larger than the applied stress on a compact even at a relative density of 0.5.

On the basis of this evidence it has been suggested that the contribution to densification by plastic flow during hot-pressing is quite small, as the contact stress is not large enough to cause the material to deform. Moreover, from the theory and experiments of self-indentation, it is well-known that a material can only deform if the contact stress is about 3 times the yield stress of the material ("yield criterion"). For this reason, workers in this field tend to assume that any contribution by plastic flow has to be very small.

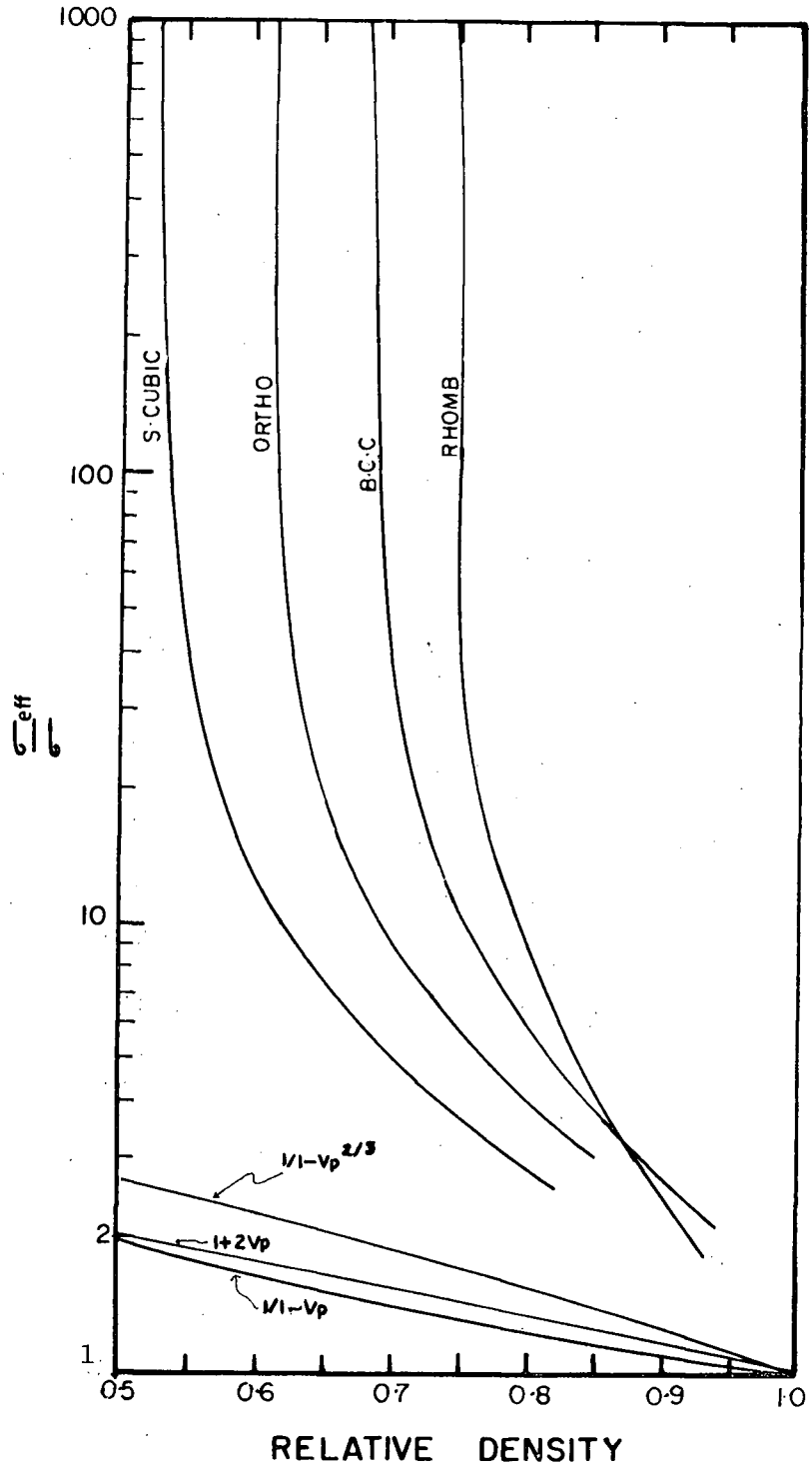

Figure 23. $\frac{\sigma_{eff}}{\sigma}$ vs. D plot for different models and also of equations used by previous workers.

However, all the equations for the effective stress, referred to above, have not been rigorously derived. All of them are either empirical or obtained from fitting experimental data into an arbitrary equation. Attempts to formulate a rigorous equation have not been very successful as the localised stresses will vary both with respect to the volume fraction of porosity and to the pore shape, which is not known. The whole problem will be further complicated if the particles in a single system are random-shaped and vary in size.

On the other hand, the problem can be simplified by assuming the particles are monosized spheres and if their geometry of packing is known. The stress is hydrostatic in nature and each shpere is being deformed at its points of contact uniformly. Under these conditions, the effective stress (σ_{eff}) with respect to the relative density of the compact is given by equation (31)

$$\sigma_{eff} = \frac{\sigma}{\alpha_1(D^{2/3}\beta^{2/3}R^2-1)}$$

The values of α_1 and β (geometric constants) have already been given in Table III for four different geometric models. The relationship between D and R was calculated using the constant volume equation and is tabulated in Appendix 1. From these the effective stress with respect to the applied stress ($\frac{\sigma_{eff}}{\sigma}$) as a function of relative density (D) has been calculated. The values are given in Appendix 3 and are plotted in Figure 23. It is quite apparent from this figure that the stress effective at the points of contact is very much larger than that assumed by previous workers. For example, below 0.79 relative density the

effective stress is more than 3 times the applied stress for all the geometric models. The instantaneous stress at the contact points of spheres is extremely high and drops very rapidly to about 10 times with an increase in relative density of less than 0.10.

From above, it is apparent that the contact stresses with respect to the applied stress in a compact are more than an order of magnitude larger than originally thought. This implies that depending upon the magnitude of the applied stress, the effective stress is reasonably high, upto a compact density of 0.85 to 0.90 (depending upon the packing geometry). If it is accepted that the packing configuration of spheres in a die approximates to the orthorhombic packing, then the effective stress is more than three times the applied stress up to 0.85 relative density of a compact.

It will be informative at this stage to analyse the magnitude and effect of contact stress in an oxide compact. Compacts of alumina are generally hot-pressed in the temperature range 1400-1700°C under a pressure of 2000 to 6000 psi. The yield stress of alumina as a function of temperature has been reported by Kronberg[15] and is shown in Table VI.

It if is considered that the hot-pressing of alumina spheres was done at 1600°C under 4000 psi and if it is considered that the packing geometry is that of the orthorhombic model, the contact stress will be in the order of 16,000 psi at 0.80 relative density of the compact, which is much more than three times the yield stress for basal slip in alumina. In the present investigation however, an end-point relative density of 0.75 was obtained at 1600°C under 4000 psi. This discrepancy may be explained from the fact that the resolved yield stress

Table V_I Yield Stress of Single Crystal Sapphire (Basal Slip)[15]

Temperature (°C)	Strain Rate (in/in/min)	Yield Stress (psi)
1400	0.05	8500
1500	0.05	6000
1600	0.05	4500
1700	0.05	3000

for the rhombohedral slip and the rhombohedral twinning are much higher than the resolved yield stress for basal slip and only 3 basal slip systems are available for the deformation of alumina under these experimental conditions.

It should be mentioned here that the effective stress calculated theoretically using equation (31) is most likely the upper limit of the stress acting on the contact faces. In practice, some of the applied stress will be lost in die-wall friction and also in creating the large flat face (indentation) on the top and bottom layer of spheres immediately after the application of load, as has been observed by Kakar.[13] Thus, it is possible that the effective stress in any particular system may not be as high as that predicted by equation (31).

V.2. Activation Energy Study

An Arrhenius type of equation can be written for the constants A in equation (32) as follows

$$A = A' \exp(-Q/RT)$$

where A' is a temperature independent constant and Q is the activation energy for the process, R and T have their usual meaning.

From the slope of a ln A vs. 1/T plot, the activation energy for the process can be obtained. These plots for lead and nickel are shown in Figures 24 and 25, respectively. For these plots, the value 'A' for lead at 200°C and that of nickel at 700°C were obtained from the experimental densification curve. As can be seen from these figures, these values of 'A' (back calculated from the densification data) lie on the straight line drawn through the other points. The

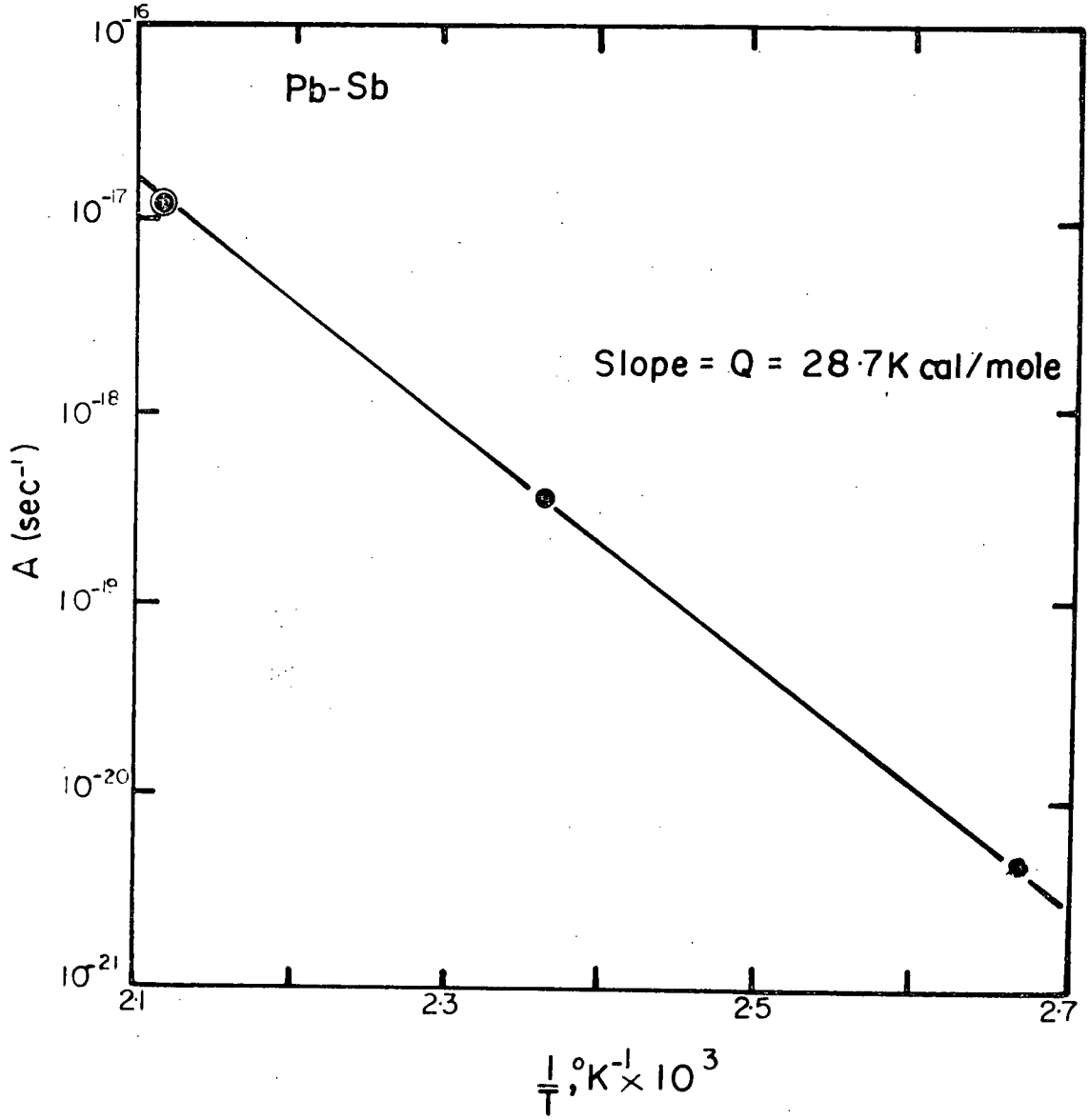

Figure 24. ln A vs. 1/T plot for Pb-2% Sb (the point represented by a dot with a ring is from the densification curve at 200°C).

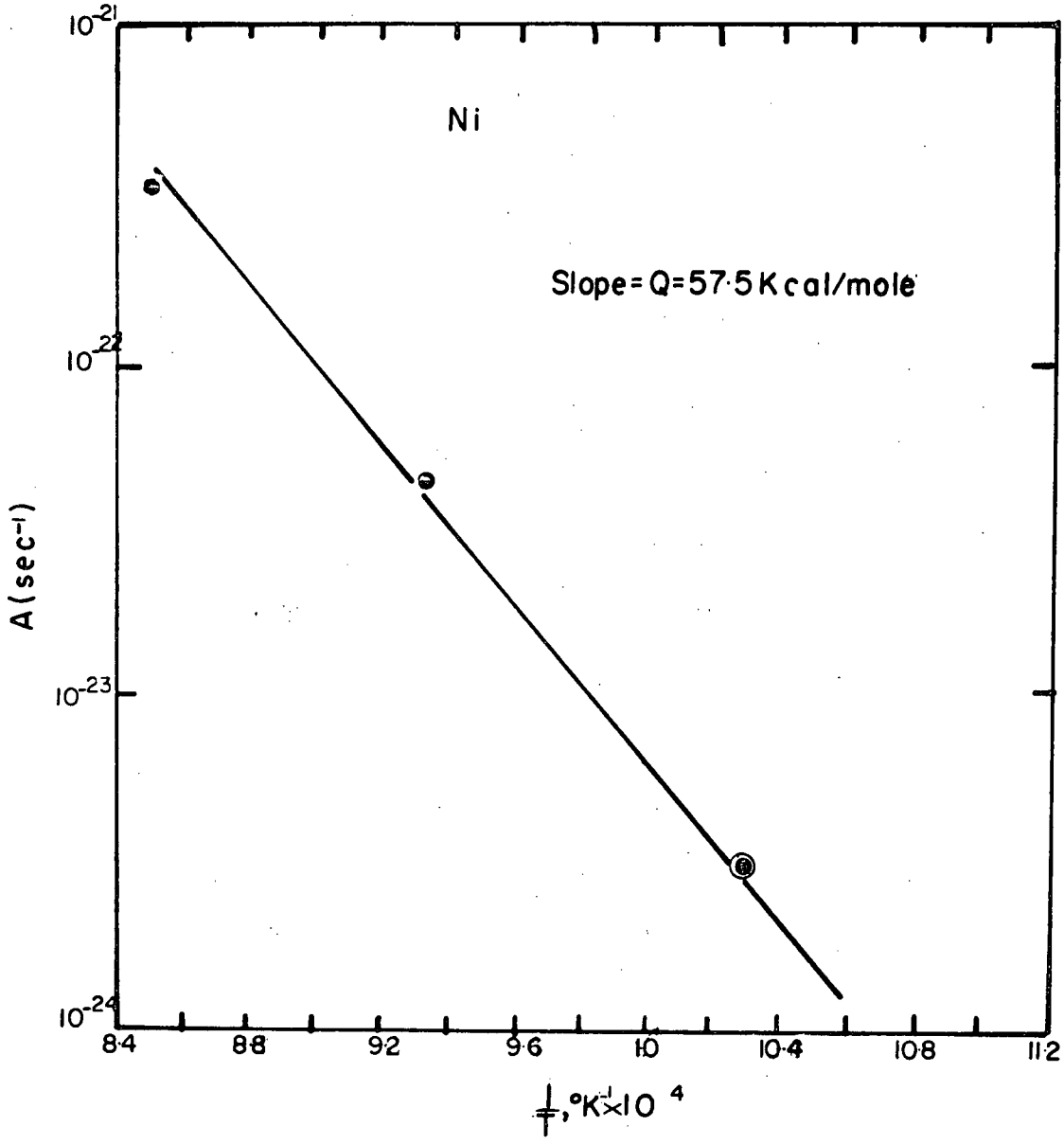

Figure 25. ln A vs. 1/T plot for Ni (the point represented by a dot with a ring is from the densification curve at 700°C).

activation energy obtained from Figure 24 for lead was 28.7 Kcal/mole which is close to the activation energy for self-diffusion of lead (26.9 Kcal/mole). Similarly the activation energy calculated from Figure 25 for nickel was 57.5 Kcal/mole. This value is also close to the activation energy for hot-working of nickel (71 Kcal/mole).[11]

V.3. Packing and Deformation Geometry Inside a Die

V.3.a. Packing Geometry

It is seen from all the Figures 14, 15 and 16 that the experimental data follows closely the theoretically derived equation for the hexagonal prism model. This agreement indicates that the overall packing geometry of monosized spheres in a die may be similar to the orthorhombic packing.

When a die is randomly filled with monosized spheres, with intermittent shaking and tapping in order to achieve a uniform packing the spheres tend to spread laterally to achieve the most stable configuration. However, the die-wall offers resistance to lateral spreading. As a result, a certain degree of stability in packing is maintained in spite of an unstable configuration. McGeary[18] studied the various modes of filling the die and the effect of container size on packing density. His results are shown in Figure 26. When the ratio of the die diameter to the sphere diameter is greater than 10, the packing density of the compact reaches a maximum of 62.5% of the theoretical density. This value is close to the as-compacted density for the orthorhombic packing.

Smith, Foote and Busang[24] studied the coordination number of spheres

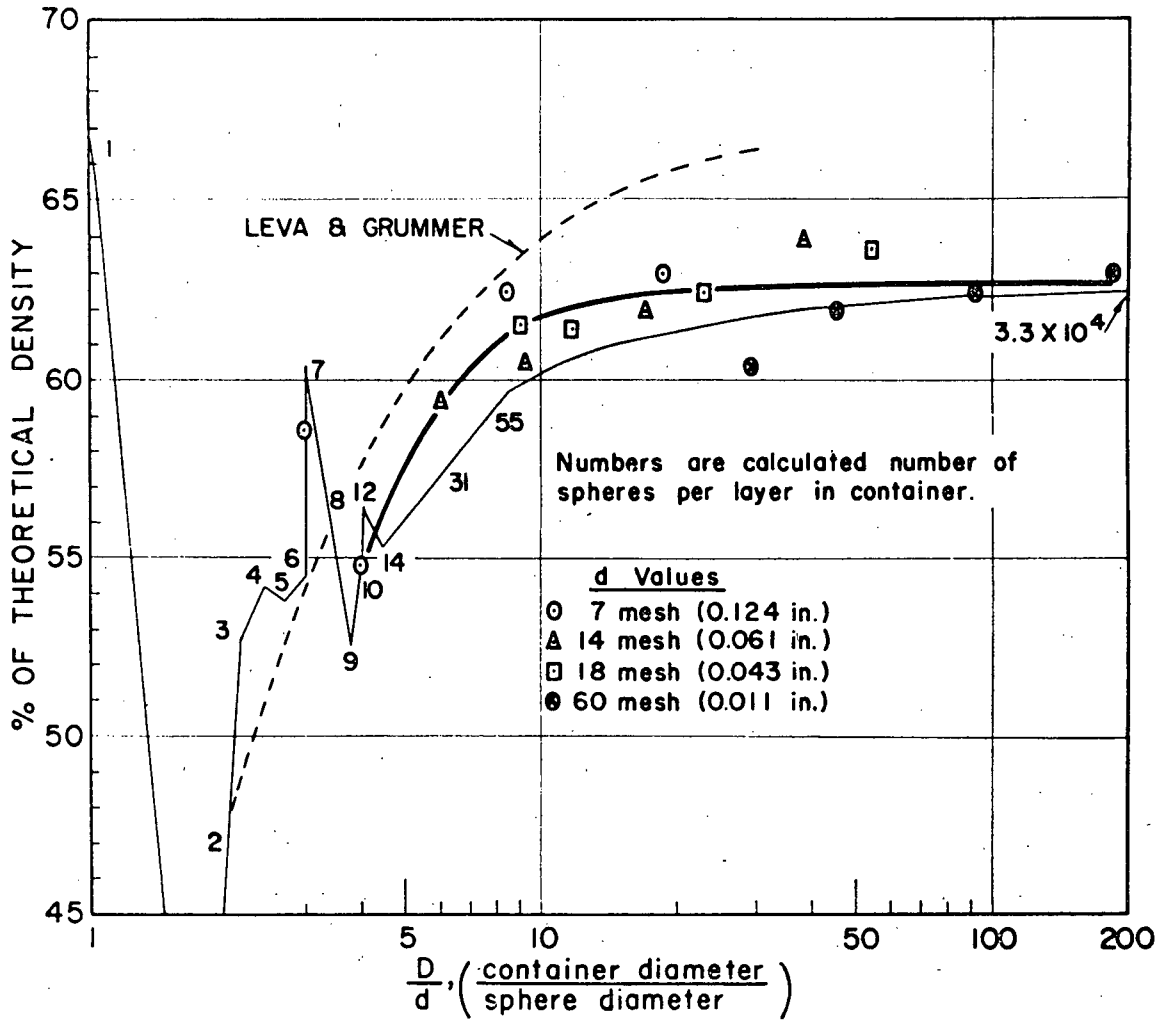

Figure 26. Effect of container size on the efficiency of packing one-size spheres (after McGeary[18]).

in a die after shaking and tapping. Their results showed a Gaussian distribution of the number of sphere with a given coordination number. The average coordination number of the sphere was close to 8. These results further confirm that the overall packing geometry in a die approximates to that of the orthorhombic model.

V.3.b. Deformation Geometry

The width of the die does not permit an integral number of spheres across the diameter; hence the ideal packing discussed in the above section does not exist across the diameter of the die since a certain number of spheres are lightly held against the die-wall. The loosely held spheres would rearrange as soon as a load is applied, resulting in a higher relative density. As no fragmentation was observed in metal compacts this increase in density can be attributed to particle rearrangement. However, in the case of sapphire (Al_2O_3) some fragmentation was noted after the experiments. This fragmentation associated with rearrangement might have contributed to densification at the initial stage. In addition, Kakar[13] observed an increase in the average coordination number of deformed spheres of lead, as the bulk density of a compact of lead spheres was increased during hot-pressing as shown in Figure 27. This indicates that particle rearrangement occurs as densification of a powder-compact proceeds, especially at the initial stage of compaction.

On further loading, the particles begin to deform. Although individual colonies of rhombohedral or tetragonal deformation were observed, the majority of the spheres showed a hexagonal prism model of deformation.

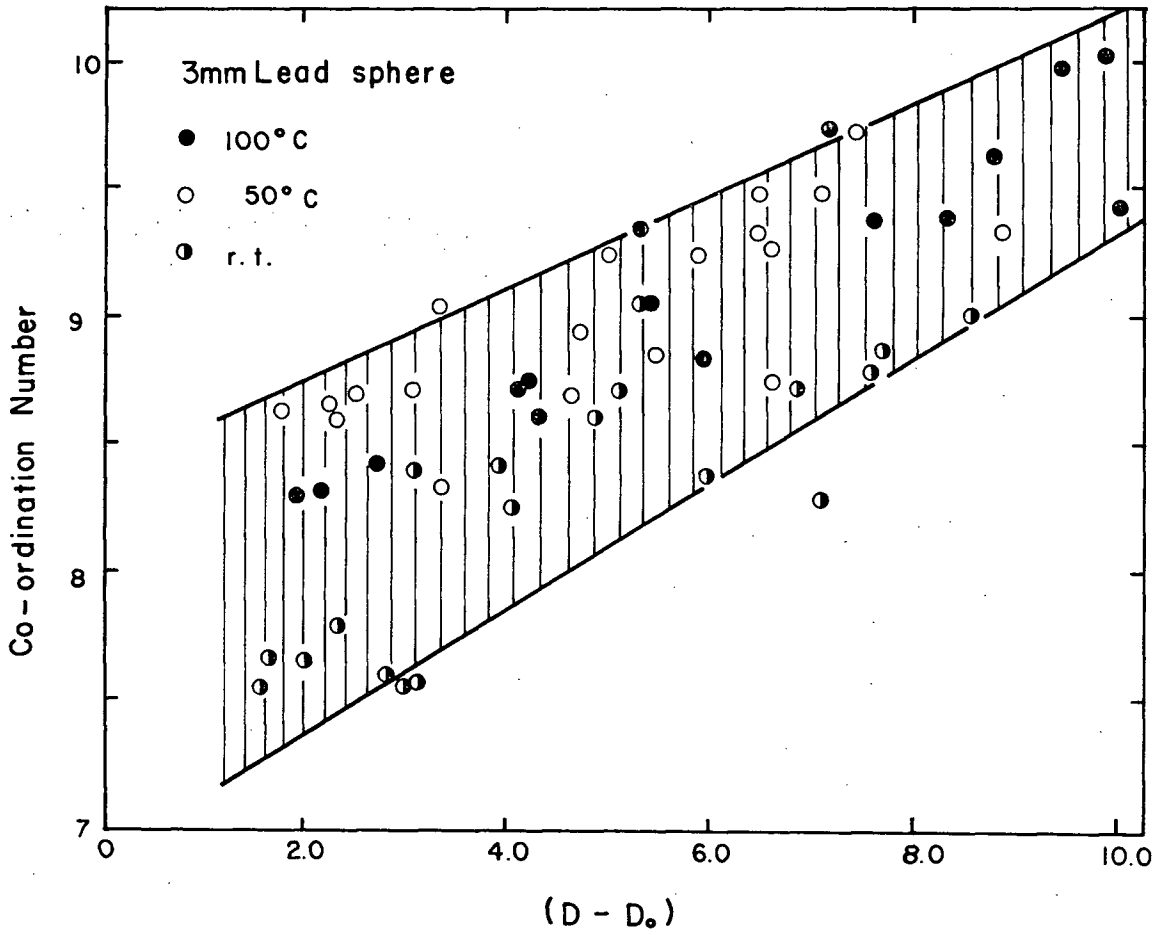

Figure 27. Coordination number vs. $(D - D_o)$ for Pb-2% Sb at various temperatures (after Kakar[13]).

This is reavealed in Figures 28 and 29 which represent nickel spheres deformed at 800 and 900°C. As can be seen from the figures, the coordination in one plane during deformation is 6 and the deformed sphere took the form of a hexagonal prism.

It has already been noted in the density vs. time curves that there is a disagreement between the theoretical curves and experimental data, particularly at the initial stage of compaction. This disagreement can be explained from the arguments above.

In the theoretical derivation, no consideration was given to account for any increase in density due to the change of coordination number. There is experimental evidence in this study and also reported by Kakar and Chaklader,[12] that particle rearrangement and fragmentation (for oxides) are significant contributing factors to densification at the initial stage of hot-pressing. This is especially true immediately after the application of load when the effective stress at the points of contact may be very high.

The experimentally observed increase in density, in the first few minutes of compaction which was always greater than the theoretically predicted increase, may be explained as follows: In the initial stage of hot-pressing, the increase in density is due to two factors (i) indentation at the points of contact and (ii) particle rearrangement leading to a higher average coordination number per sphere. It has not been possible at present to incorporate the increase in density due to the second effect, into the theoretical equations. In addition, to account for the deviation, the effect of the existence of very high strain rates, at the initial stage of hot pressing, (as seen experimentally), should be taken into consideration.

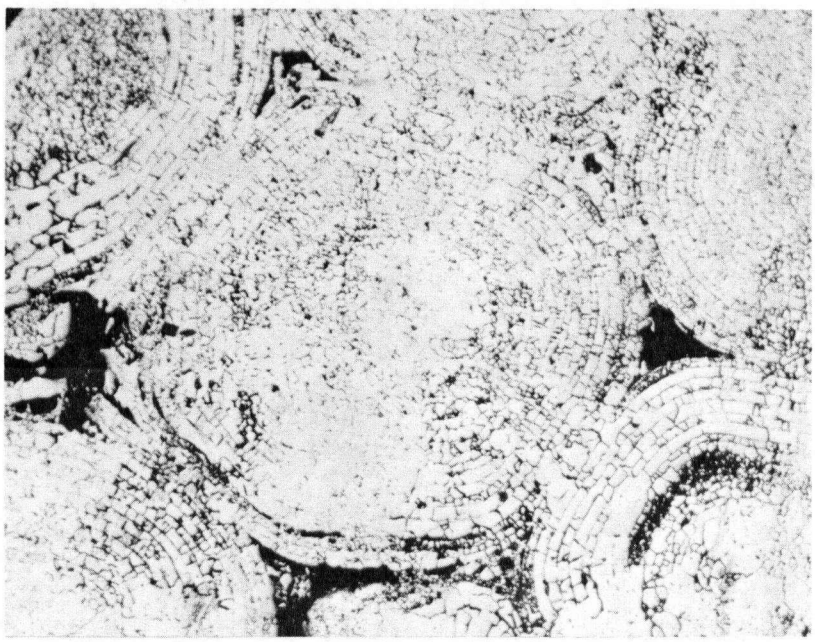

Figure 28. Microstructure of Ni spheres hot-pressed at 800°C and 2162 psi. (80x)

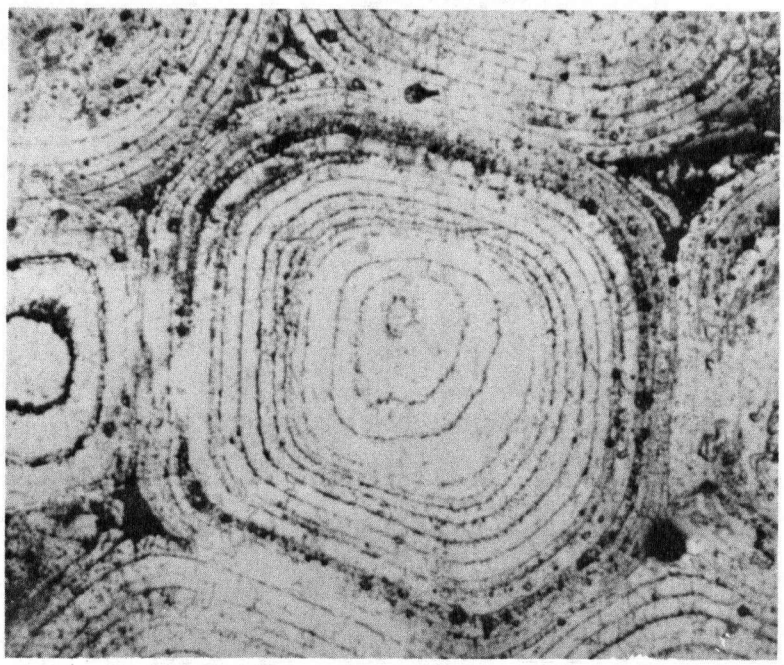

Figure 29. Microstructure of Ni spheres hot-pressed at 900°C and 1477 psi. (95x)

V.4 Limitations of the Present Analysis

1. In the theoretical consideration, the stress is considered to be hydrostatic, but in practice a uniaxial stress is applied in hot-pressing. However, due to the existence of back stress from the die-wall and the other plunger, the stress may be assumed to be isotropic However, this assumption may not be a good one in practice.

2. Although the same heat-treatments were given for the balls used in hot-pressing and the specimens used in hot-compression, the structure of these may not be the same. Since the constant 'A' is a function of structure, the values are subjected to unknown error.

3. In the hot-compression of Pb-Sb and Ni specimens, the friction between specimen and the alumina buttons was not taken into consideration. This may give rise to some errors in evaluating the value of steady-state stress and hence the values of 'A' and 'n'.

4. The compostion of the Pb-Sb alloy was originally considered to be Pb-2% Sb (manufacturer's composition) but it was found later that it was actually Pb-15% Sb. Since this is a hyper-eutectic alloy,the power law dependence of steady-state strain rate on stress, giving the values of 'A' and 'n' shown in Table IV may not be completely valid. However, in the temperature and strain rate range used in this investigation, super-plastic behaviour would not be expected, and it has been assumed the values of 'A' and 'n' are reliable from the compression tests.

5. In the theory, the bulk strain-rate within the compact is used, based on the instaneous density. It would be more correct to consider

the strain-rate localised in the contact areas, if it were possible to characterise it. The error introduced in this way is unknown, but is not believed to be appreciable beyond the early stages of densification.

CHAPTER VI

SUMMARY AND CONCLUSIONS

Isothermal densification curves of a powder compact during hot-pressing have been theoretically calculated using the geometry of deformation of particles and hot-compression data. The particles are assumed to be monosized spheres. Four different deformation models were considered: Cubic (Z = 6), orthorhombic (Z = 8), b.c.c. (Z = 8), and rhombohedral (Z = 12) where Z is the coordination of the sphere. For hot-compression an equation of type $\dot{\varepsilon} = A\sigma^n$ was used. The final densification equation relating the relative density and time for different ideal packing arrangements has been derived which is

$$\int_{D_o}^{D_{max}} D^{-1}\{D^{2/3}\beta^{2/3}R^2-1\}^n \, dD = \int_o^t A\left(\frac{\sigma}{\alpha_1}\right)^n dt$$

The equation was solved in a computer to obtain the theoretical plots. However, in order to use this equation the values for material constants (A and n) were necessary and were determined by hot-compression tests in an Instron machine. Three different materials were used for this purpose - these are Pb-2% Sb, Ni and Al_2O_3. Theoretical curves for all four different geometric models were generated by the computer.

These theoretical curves were compared with hot-pressing data of spheres of the same materials at different temperatures and pressures.

The following conclusions can be made

(1) The general theoretical equation proposed is found to be obeyed by the spherical particles during the intermediate stage of hot-pressing.

(2) The experimental points follow closely the theoretically predicted curve for the hexagonal prismatic deformation model.

(3) This indicates the overall packing geometry of sphere inside the die coincides with the orthorhombic packing in agreement with the observation of previous workers.

(4) A deviation was encountered at the initial stage of densification, which could be explained from particle rearrangement at the beginning of hot-pressing as was observed in this study and by other workers previously.

A theoretical equation for calculating the effective stress acting on the contact faces in a compact of spheres has been derived. This is:

$$\sigma_{eff} = \frac{\sigma_{app}}{\alpha_1 (D^{2/3}\beta^{2/3}R^2 - 1)}$$

Theoretical plots of relative effective stress as a function relative density were computed for 4 different geometric models. When these are compared with the effective stress plots used by previous workers, it was observed that the actual effective stress is very much higher than that considered so far.

From above, it is concluded that the contribution to densification during hot-pressing by plastic flow is more than that considered by previous investigators.

CHAPTER VII

SUGGESTIONS FOR FUTURE WORK

1. Metallographic study of hot-pressed compacts should be done for checking the change of R with respect to change in D in a die as R is a very critical function for effective stress. The experimentally determined R should be compared with the theoretical R and necessary correction to the densification equation should be made for better understanding.

2. The values of effective stress at different stages of densification should also be evaluated experimentally. This can be done by using hemispherical specimens.

3. From the above experiment the yield criterion at an elevated temperature should be checked. (Yield criterion refers to "Stress required to deform by self-indentation is 3 times the yield stress".)

4. If strain rate dependence on stress is given by $\dot{\varepsilon} = A\{\text{Sin h}(\alpha_2\sigma_1)\}^n$, one can write a densification equation by following the same treatment as done in Chapter II, as follows

$$\int_{D_o}^{D_{max}} D^{-1} \quad \text{Sin h}\left[\frac{\alpha_2}{\alpha_1} \cdot \frac{\sigma}{(D^{2/3}\beta^{2/3}R^2-1)}\right]^{-n} dD = \int_0^t A\, dt$$

A computer programme for this is given in Appendix 5. By knowing the constants A, α_2 and n for different materials, the validity of this equation should be determined.

APPENDICES

APPENDIX 1

A. Theoretical Calculations

1. Cubic Model

R	Bulk Density (%)
0.620350	52.360
0.620352	52.556
0.620374	53.149
0.620469	54.145
0.620728	55.565
0.621282	57.423
0.622307	59.749
0.624038	62.576
0.626787	65.937
0.630972	69.869
0.637180	74.393
0.646268	79.498
0.659573	85.085
0.679356	90.843
0.709891	95.936
0.715532	96.506

2. Hexagonal Prismatic and Tetrakaidecahedron Models

R	Bulk Density (%) Hex. Prism.	Bulk Density (%) b.c.c. model
0.620350	60.460	68.017
0.620352	60.687	68.273
0.620382	61.369	69.040
0.620509	62.511	70.325
0.620854	64.121	72.137
0.621593	66.207	74.483
0.622964	68.774	77.371
0.625287	71.824	80.802
0.628993	75.340	84.757
0.634679	79.272	89.181
0.643213	83.507	93.946

R	Bulk Density (%) [Z = 14]
0.669404	99.450

3. Rhombic Dodecahedron Model

R	Bulk Density (%)
0.620350	74.048
0.620353	74.325
0.620397	75.156
0.620588	76.531
0.621107	78.437
0.622218	80.842
0.624288	83.697
0.627815	86.908
0.633499	90.317
0.642361	93.646
0.655600	96.410

APPENDIX 2

A. Hot-Compression Data

1. Lead-2% Antimony - 100°C

$\dot{\varepsilon}$ (sec^{-1})	σ (psi)
3.9401×10^{-5}	5257
9.8502×10^{-5}	6507
1.9700×10^{-4}	7646
3.9401×10^{-4}	8986

2. Lead-2% Antimony - 150°C

$\dot{\varepsilon}$ (sec^{-1})	σ (psi)
3.4972×10^{-5}	1934
8.7443×10^{-5}	2398
1.6666×10^{-4}	2797
2.9682×10^{-4}	3195

3. Nickel - 800°C

$\dot{\varepsilon}$ (sec^{-1})	σ (psi)
3.4904×10^{-5}	6387
7.4904×10^{-5}	7461
1.5873×10^{-4}	8817
2.9629×10^{-4}	10070

4. Nickel - 900°C

$\dot{\varepsilon}$ (sec^{-1})	σ (psi)
2.6666×10^{-5}	3914
9.8619×10^{-5}	5171
1.7543×10^{-4}	5845
2.7777×10^{-4}	6446

APPENDIX 3

A. Effective Stress for Different Models

1. Cubic Model

D	$\frac{\sigma_{effective}}{\sigma_{applied}}$
0.52	2666
0.53	120
0.55	30.22
0.59	12.80
0.62	9.08
0.65	6.66
0.69	5.0
0.74	3.81
0.79	2.93
0.85	2.25

2. Hexagonal Prism Model

D	$\frac{\sigma_{effective}}{\sigma_{applied}}$
0.60	2414
0.61	104.3
0.62	46.9
0.64	26.1
0.66	16.41
0.68	11.68
0.71	7.8
0.75	5.769
0.79	4.33
0.83	3.3

3. B.C.C. Model

D	$\frac{\sigma_{effective}}{\sigma_{applied}}$
0.68	1557
0.69	69
0.70	31.2
0.72	17.42
0.74	10.93
0.77	7.39
0.80	5.2
0.84	3.8
0.89	2.8
0.93	2.2
0.99	1.46

4. Rhombic Dodecahedron Model

D	$\frac{\sigma_{effective}}{\sigma_{applied}}$
0.74	959.5
0.75	42
0.76	19.14
0.78	9.882
0.80	6.69
0.83	4.52
0.86	3.210
0.90	2.355
0.93	1.774
0.96	1.354

APPENDIX 4

STRAIN RATES AT DIFFERENT STAGES OF DENSIFICATION

1. (a) Lead-2% Antimony - 100°C, 918 psi

Relative Density (D)	Strain Rate (sec^{-1})
0.64	1.017×10^{-2}
0.66	1.449×10^{-3}
0.68	2.785×10^{-4}
0.71	6.376×10^{-5}
0.75	1.796×10^{-5}

(b) Lead-2% Antimony - 150°C, 918 psi

Relative Density (D)	Strain Rate (sec^{-1})
0.66	1.241×10^{-1}
0.68	2.384×10^{-2}
0.71	5.459×10^{-3}
0.75	1.538×10^{-3}
0.79	4.609×10^{-4}
0.83	1.472×10^{-4}

2. (a) Nickel - 800°C, 2162 psi

Relative Density (D)	Strain Rate (sec^{-1})
0.66	3.913×10^{-2}
0.68	0.426×10^{-3}
0.71	1.278×10^{-3}
0.75	3.192×10^{-4}
0.79	8.59×10^{-5}
0.83	2.444×10^{-5}

(b) Nickel - 900°C, 2105 psi

Relative Density (D)	Strain Rate (sec^{-1})
0.66	2.551×10^{-1}
0.68	4.206×10^{-2}
0.71	8.357×10^{-3}
0.75	2.086×10^{-3}
0.79	5.575×10^{-4}
0.83	1.598×10^{-4}

3. Alumina - 1600°C, 4000 psi

Relative Density (D)	Strain Rate (sec^{-1})
0.64	2.375×10^{-2}
0.66	3.703×10^{-3}
0.68	7.716×10^{-4}
0.71	1.895×10^{-4}
0.75	5.635×10^{-5}
0.79	1.799×10^{-5}
0.83	6.071×10^{-6}

APPENDIX 5

COMPUTER PROGRAMME

```
********** PLEASE RETURN TO ELECTRICAL ENGINEERING **********
 $SIG XRSA P=8 T=1M PRIO=V
**LAST SIGNON WAS: 11:33:35   07-13-71
  USER "XRSA" SIGNED ON AT  11:32:07 ON 08-18-71
 $GET FILE1
READY.
 $LIS FILE1
      1            INTEGER STORE1, STORE2, CASE
      2            REAL N
     2.26
      3            DATA TAKE1,TAKE2,TAKE3,TAKE4/'GENE','RAL ','SPEC','IAL '/
      4            READ(5,1) N, BETA, A, SIGMA, ALPHA, DELTAT, ALPHA2
      5      1      FORMAT (2F10.4,F10.5,4F10.4)
      6            WRITE(6,1)N, BETA, A, SIGMA, ALPHA, DELTAT, ALPHA2
      7            CASE=2
      8            IF(ABS(ALPHA2).GT.0.00005)  CASE=1
      9            VALUE1 =QUEST1(TAKE1,TAKE3,CASE)
     10            VALUE2 =QUEST2(TAKE2,TAKE4,CASE)
   10.1
   10.2
     11            WRITE(6,102) VALUE1, VALUE2
     12      102   FORMAT(///40X'THIS CORRESPONDS TO THE ',2A4, 'FORMULA CASE')
     13      C NOW READ THE TABLE OF R VS D VALUES
     14            DIMENSION X(16),Y(16)
     15            DATA X,Y/16*0.0,16*0.0 /
     16            WRITE(6,32)
     17      32    FORMAT(5X,'TABLE OF D VERSUS R VALUES')
     18            DO 2 I2=1,16
     19            READ(5,3) D,R,Z
     20      3     FORMAT(3F10.4)
     21            WRITE(6,31)D,R
     22      31    FORMAT(5X,E14.7,5X,E14.7)
     23            X(I2)=D
     24            Y(I2)=R
     25            IF(Z.GT.0.1) GO TO 4
     26      2     CONTINUE
     27      4     I2MINS=I2-1
     28            JTIMES=I2MINS*2
     29            ISUM=I2
     30            DMAX=D
     31            DNOT=X(1)
     32            DELTAD=(DMAX-DNOT)/JTIMES
     33            WRITE(6,5) DMAX,DELTAD,ISUM
     34      5     FORMAT(/5X,'DMAX =',F10.4,5X,'DELTAD =',F10.5,5X,'TOTAL NUMBER OF
     35           1CARDS OF D VS R READ =',I4)
     36            SUM1=0.0
     37            D=DNOT
     38            JTIMES=JTIMES-1
     39            DO 6 I6=1,JTIMES
     40            FACT3=D*BETA
     41            FACT4=FACT3**0.667
     42            FACT1=((D*BETA)**0.667)*R*R-1.0
     43            FACT2=(FACT1**N)/D
   43.1
     44            IF(CASE.EQ.2) GO TO 150
     45            VALUE=1.0/(SINH((ALPHA2/ALPHA)*SIGMA/FACT1))**N
     46              FACT2=VALUE/D
   46.1
```

```
46.2
      150   CONTINUE
            SUM1= SUM1+FACT2*DELTAD
            D=D+DELTAD
            STORE1=1
            M=0
            DO 7 I7=1,ISUM
            IF(ABS(X(I7)-D).LE.0.0002) M=I7
            IF(X(I7).LT.D) STORE1=I7
            IF(X(I7).GT.D) GO TO 9
      7     CONTINUE
            GO TO 10
      9     STORE2=I7
      10    IF(M.EQ.0) GO TO 11
            R=Y(M)
            GO TO 12
      11    DELT = D-X(STORE1)
            R=Y(STORE1)+(Y(STORE2)-Y(STORE1))*DELT /(X(STORE2)-X(STORE1))
            WRITE(6,109) D,R
      109   FORMAT(/'D='F10.7,5X,'R=',F10.7)
      12    WRITE(6,13) SUM1
      6     CONTINUE
      13    FORMAT('SUM1='E16.9)
            CONS=A*((SIGMA/ALPHA)**N)*(10.**(-20))
            IF(CASE.EQ.1) CONS=A*(10.**(-8))
            SUM2=0.0
            FACT =   SUM1/(CONS*DELTAT)
            NCOUNT=0
            DO 152 I152=1,100
            IF(FACT.LT.(1000.0)) GO TO 151
            FACT = FACT/10.0
            NCOUNT=NCOUNT+1
      152   CONTINUE
      151   NLIM =FACT
            IF(NLIM.LT.4) NLIM=4
            NL1 =NLIM/4
            IF(NL1.LT.2) NL1=1
            DO 14 I14=1,NLIM,NL1
            TIME=I14*DELTAT *(10.**NCOUNT)
            SUM2=TIME*CONS
            WRITE(6,16)TIME,SUM2
      16    FORMAT(/'TIME='E12.5,5X,'SUM2=',E12.5)
      14    CONTINUE
            STOP
            END
            FUNCTION QUEST1(TAKE1,TAKE3,CASE)
      91.1  INTEGER CASE
            QUEST1=TAKE1
            IF(CASE.EQ.2)QUEST1=TAKE3
            RETURN
            END
            FUNCTION QUEST2(TAKE2,TAKE4,CASE)
      96.1  INTEGER CASE
            QUEST2=TAKE2
            IF(CASE.EQ.2) QUEST2=TAKE4
            RETURN
            END
END OF FILE
```

BIBLIOGRAPHY

1. R. Chang and C.G. Rhodes, J. Am. Ceram. Soc., 45, 379 (1962).
2. R.L. Coble and J.S. Ellis, J. Am. Ceram. Soc., 46, 438-41 (1963).
3. R.L. Coble, in "Sintering and Related Phenomena", Ed., G.C. Kuezynski, N.A. Hooton and C.F. Gibbon (Gordon and Breach, Science Publishers, New York), (1967), p. 329.
4. R.L. Coble, J. App. Phys., 41, 4798 (1970).
5. P.L. Farnsworth and R.L. Coble, J. Am. Ceram. Soc., 49, 264 (1966).
6. E.J. Felten, J. Am. Ceram. Soc., 44, 381, (1961).
7. G.M. Fryer, Trans. Brit. Ceram. Soc., 66, 127 (1967) and 68, 181-185 (1969).
8. J.K. Mackenzie and R. Shuttleworth, Proc. Phys. Soc. (London), B, 62, 833-852 (1949).
9. H. Hencky, Z. Angew. Math. Mech., 3, 241 (1923).
10. J. Ishlinsky, J. App. Math. Mech. U.S.S.R., 8, 233 (1944).
11. J.J. Jonas, C.M. Sellars and W.J. McG. Tegart, in "Metallurgical Reviews", vol. 14, Review 130, 1 (1969).
12. A.K. Kakar and A.C.D. Chaklader, J. App. Phys., 38, 3223-30 (1967).
13. A.K. Kakar "Deformation Theory of Hot-Pressing", Ph.D. Thesis, Department of Metallurgy, University of British Columbia (1967).
14. M.S. Koval'Chenko and G.V.Samsonov, Poroshkovaya Met., 1, 3 (1961).
15. M.L. Kronberg, J. Am. Ceram. Soc., 45, 6, 274 (1962).
16. G.E. Mangsen, W.A. Lambertson and B. Best, J. Am. Ceram. Soc., 43, 55 (1960).

17. J.D. McClelland, in "Powder Metallurgy Proceedings of International Conference, New York, 1960, W. Leszynski, Ed. (Interscience Publishers, New York, 1961).

18. R.K. McGeary, J. Am. Ceram. Soc., 44, 513 (1961).

19. P. Murray, D.T. Livey and J. Williams, in"Ceramic Fabrication Process", W.D. Kingery, Ed. (Technology Press Cambridge, Mass., and John Wiley and Sons, Inc., New York, 1958).

20. F.R.N. Nabarro, in the "Strength of Solids", London (Physical Society), 75 (1948).

21. R.C. Rossi and R.M. Fulrath, J. Am. Ceram. Soc., 48, 558-64 (1965).

22. D.R. Rummler and H. Palmour, J. Am. Ceram. Soc., 51, no. 6, 320 (1968).

23. S. Scholz and B. Lersmacher, Arch. Eisenhuettenw, 41, 98 (1964).

24. W.O. Smith, P.D. Foote and P.F. Busang, Phys. Rev., 34, 1272 (1929).

25. T. Vasilos, J. Am. Ceram. Soc., 43, no. 10, 517 (1960).

26. T. Vasilos and R.M. Spriggs, J. Am. Ceram. Soc., 46, 493-96 (1963).

27. S.I. Warshaw and F.H. Norton, J. Am. Ceram. Soc., 45, 479 (1962).